EXPERIMENTAL HEAT TRANSFER
2025, VOL. 38, NO. 7, 848–880
https://doi.org/10.1080/08916152.2024.2424820

Taylor & Francis
Taylor & Francis Group



# Endwall film-cooling in a cascade with filleted vane, upstream discrete slots, and holes

Adeola S. Shote[a,b], Barbara B. Huyssen[a], and Gazi I. Mahmood[a,c]

[a]Department of Mechanical and Aeronautical Engineering, University of Pretoria, Pretoria, South Africa; [b]Department of Mechanical Engineering, Olabisi Onabanjo University, Ago-Iwoye, Nigeria; [c]Department of Mechanical Engineering, Prince Mohammad Bin Fahd University, Al Khobar, Saudi Arabia

**ABSTRACT**

In vane cascades, large filleted vanes influence aerodynamics, while upstream endwall film-cooling arrangement impacts aero-thermal performance. This study explores experimental investigations on endwall flows and film-cooling effectiveness in a filleted vane cascade using discrete slots and holes. Two fillet profiles are examined covering the leading-edge area to either the throat or 62% of the axial chord. Film-cooling employs two slots and two rows of holes in the leading-edge region with inlet blowing ratios ranging from 1.0 to 2.8. Results show variations in total pressure loss and Nusselt number between filleted and un-filleted vanes, highlighting optimal film-cooling effectiveness with the smaller fillet profiles.

**ARTICLE HISTORY**
Received 30 June 2024
Accepted 28 October 2024

**KEYWORDS**
Passage-vortex; endwall heat transfer; film-cooling effectiveness; total pressure-loss; film-cooling distributions

## Introduction

In the field of gas turbine development, researchers often introduce geometric modifications to vane or blade cascades. These modifications, including fillets, contoured endwalls, and film-cooling holes, aim to reduce aerodynamic losses and wall heat transfer, and improve film-cooling effectiveness. However, not all modifications yield consistent results. Some enhance aero-thermal performance but fall short in film-cooling performance, while others excel in film-cooling performance but underperform in aero-thermal aspects.

The film-cooling flow rate is a critical factor, as it directly impacts the load on compressors responsible for supplying film-cooling air in operational gas turbines. In the present experimental study, it is presented the investigation of the effects of fillet profiles on endwall heat transfer and upstream combined discrete slots and holes film-cooling effectiveness.

Several studies have demonstrated the potential of energizing secondary flows through air injection, leading to innovative combinations of mainstream and injected flows with various blade leading edges and endwall geometries in a linear cascade.

Using a leading-edge fillet can effectively reduce aerodynamic losses by weakening the horseshoe vortex. The fillet creates a smooth transition from the nozzle guide vane's leading edge to the endwall, mitigating the strength of the vortex that forms at this junction [1]. When film cooling is employed, filleted vanes can lead to a reduction in total-pressure losses, especially at high coolant mass fluxes [2]. Nonetheless, larger fillet radii can lead to increased aerodynamic loss in the boundary layer, affecting turbine efficiency. Therefore, while fillets are used to improve the flow transition at the blade root, their size must be optimized to balance the reduction in vortex strength against the potential increase in aerodynamic losses. Zhang

**CONTACT** Barbara B. Huyssen Barbara.huyssen@up.ac.za Department of Mechanical and Aeronautical Engineering, University of Pretoria, Engineering I building, Hatfield campus, Lynnwood Road, Hatfield, Pretoria 0028, South Africa

et al. [3] investigated the impact of various leading-edge fillet geometries on diffused hole film-cooling effectiveness, noting significant effects near the vane-endwall junction. Among long, medium, and short fillet geometries, the long fillet showed greater control over the suction side leg of the horseshoe vortex. Mahmood and Arnachellan [4, 5] and Shote et al. [6] explored the film-cooling efficacy on the GE–E3 nozzle guide vane's endwall via experimental methods. Introducing fillets at the upstream slot can change the velocity distribution of the slot coolant, leading to increased adiabatic cooling effectiveness and a larger effective cooling area. Their findings showed that secondary flow patterns developed along the vane passage, with the endwall boundary layer being elevated by passage vortices, thus enhancing heat transfer near the pressure side. However, this elevation limited the downstream presence and coverage of upstream coolant, particularly when the blowing ratio was under two, resulting in diminished film-cooling effectiveness on the pressure side.

Previous research by Thomas and Povey [7], and Ornano and Povey [8], within a filleted vane cascade featuring cylindrical holes on an upstream endwall, revealed that the holes' positioning and angling, along with the coolant to mainstream mass flow ratio, significantly impacted film-cooling effectiveness, coolant trajectory, and secondary flow behavior in the cascade passage.

Research by [9, 10] compared adiabatic film-cooling effectiveness using cylindrical cooling holes versus fan-shaped cooling holes in linear vane cascades. The results indicated that fan-shaped holes distributed effectiveness more evenly and reduced total pressure losses compared to cylindrical holes. Additionally, Barigozzi et al. [11] explored the impact of exit area variations in four rows of fan-shaped film-cooling holes within a vane cascade. Smaller exit areas led to reduced aerodynamic losses, while larger exit areas improved local cooling effectiveness. Wang et al. [12] extended the investigation by employing multiple rows of cylindrical holes both upstream and inside the passage of a vane cascade, with the upstream holes dominating the endwall film-cooling effectiveness.

Thole and Knost's experimental work [13] in a vane cascade with an upstream slot and discrete cooling holes revealed insights into local heat transfer and film-cooling effectiveness on the endwall. Utilizing only the upstream slot left the pressure-side regions largely uncooled, whereas combining the slot with holes achieved a more extensive lateral spread of film-cooling on the endwall. Computational studies by Hada and Thole [14], and Du and Li [15], compared film-cooling effectiveness distributions along the vane cascade endwall using continuous upstream slots with varying geometries. Their findings suggested that a slightly elevated upstream endwall of the slot could enhance coolant spread, compared to a flat upstream endwall configuration. The combined film-cooling flow from the upstream discrete holes and a continuous slot of Barigozzi et al. [16] provided desirable results in the vane cascade when a blockade was introduced upstream in the mid-pitch location. Tao et al. [17] noted that increasing the blowing ratio, positioning slots near the vane's leading edge, and increasing the slot angle boosted endwall film-cooling effectiveness and dampened secondary flows within the cascade passage. Sundaram and Thole [18] found that embedding discrete film-cooling holes within a trench on the upstream endwall improved film-cooling effectiveness, as the cooling jets adhered to the endwall.

Gao at al. [19] and Thrift et al. [20] observed that positioning and angling the continuous slot of film-cooling flow correctly led to reduced endwall heat transfer and enhanced film-cooling effectiveness. Laveau et al. [21] and Kang et al. [22] reported high heat transfer in areas with intense endwall secondary flows.

In the current study, film-cooling through discrete slots is shown to offer aerodynamic benefits with coolant flows similar to those in discrete hole configurations, as documented in references [4–6]. Consequently, this experiment incorporates both discrete slots and cylindrical holes to examine film-cooling in conjunction with a filleted vane. The findings, including measurements of pressure losses, endwall heat transfer coefficients, and endwall film-cooling effectiveness, are detailed to demonstrate the impact of the vane's fillet design and the coolant's mass flux on the system's performance.

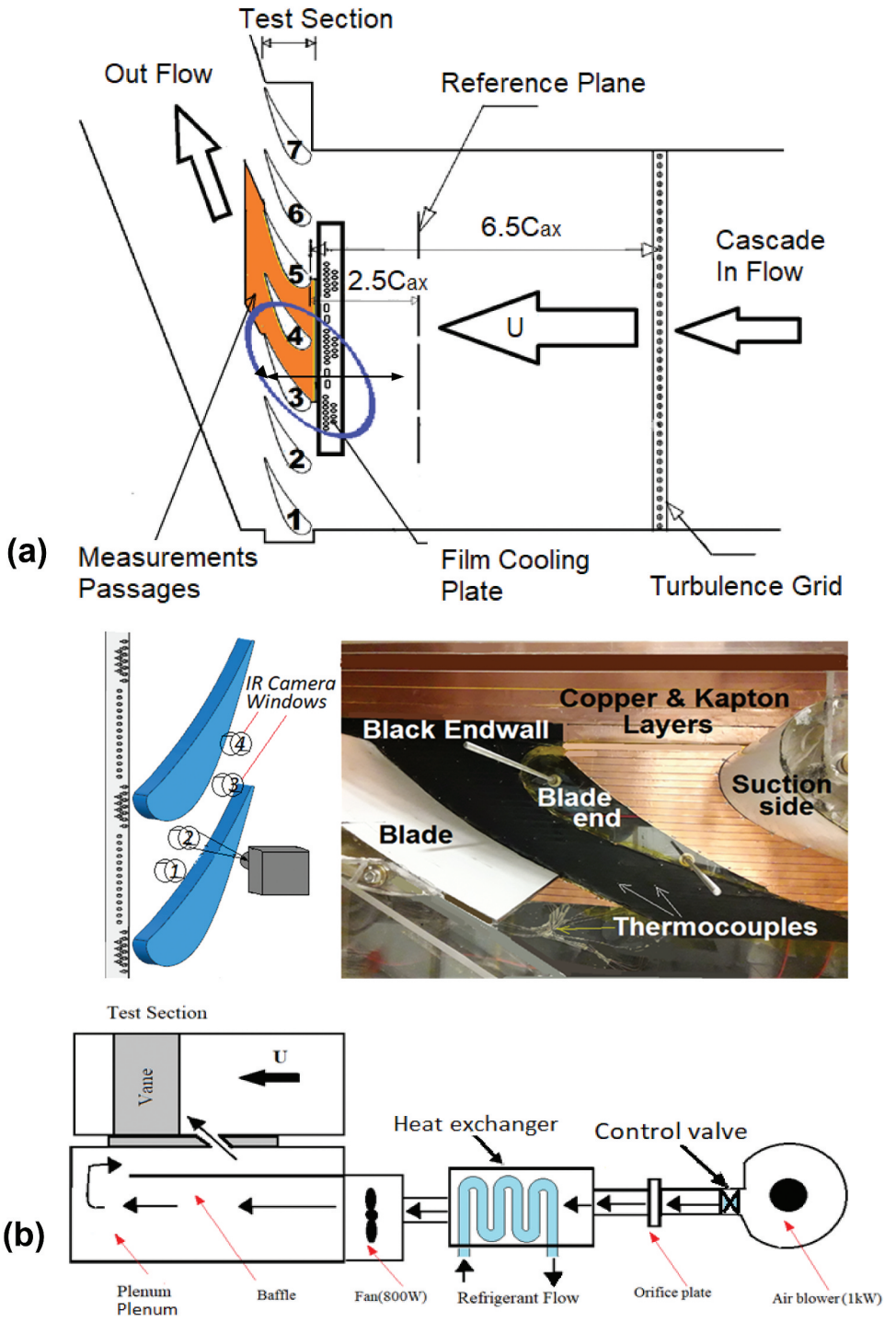


**Figure 1.** (a) Schematic of plan view of cascade test facility in the atmospheric wind tunnel, and (b) flow line diagram for the film-cooling.

**Table 1.** Geometric parameters of vane cascade.

| Incidence | $C_{ax}$ (m) | C (m) | C/S | C/P |
|---|---|---|---|---|
| 0° | 0.203 | 0.355 | 1.479 | 1.328 |

## Experimental facility and methods

The experimental investigations take place in a low-speed cascade housed within an atmospheric wind tunnel (as depicted in Figure 1(a)). The cascade consists of 7 two-dimensional blades, designed by using the hub-side profile of a nozzle guide vane from the gas turbine engine referenced in [23]. For detailed cascade geometry, refer to Table 1.

The open-circuit wind tunnel generates flow using two large duct fans connected in series. To induce turbulence in the incoming flow, a grid of cylindrical rods is employed at 6.5 chord lengths upstream of the cascade inlet. The reference properties of the flow field, obtained in a plane situated 2.5 $C_{ax}$ upstream the cascade and 4.0 $C_{ax}$ downstream of the turbulence grid (refer to Figure 1), are summarized in Table 2. The Reynolds number ($Re$) in the table is estimated based on the reference velocity ($U$) and vane profile chord length, $C$. The reference flow properties listed in Table 2 are gauged within the pitchwise plane showcased in Figure 2(a). This measurement employs a commercial pitot-static pressure probe with 1.6 mm tip, alongside a hot-wire probe (operating on a constant current single wire principle), and a thermal probe. The latter is inserted through a cutout slot positioned at the height of the fourth leading-edge (LE) blade. The freestream velocity, turbulence intensity, and temperature ($T_r$) are reported above the boundary layer of the bottom endwall. The turbulence length-scale of 2.3d is derived from the diameter ($d$) of the turbulence grid rods. For comprehensive details on the test facility and geometric parameters, refer to Ref [24].

Considering the small pressure drop across the cascade, the flow condition is treated as incompressible. The cascade features cutout slots on the top endwall, drilled holes in the bottom endwall, and static pressure taps on the vane surface. These allow for the insertion of probes to measure velocity, temperature, and pressure within the cascade.

To supply film-cooling flow in the cascade, a secondary flow circuit (depicted in Figure 1(b)) is employed on the outside of the bottom endwall in the test section. Two fans, with power ratings of 1 kW and 800 W, drive the flow in the secondary flow line. The heat exchanger in Figure 1(b) is a chiller unit of a vapor-compression system and controls the film-cooling flow temperature.

To control the coolant flow, a valve is utilized within the flow circuit. Additionally, a metered pipe section equipped with a calibrated orifice plate measures the coolant flow rate (details provided in Ref [24]). The plenum, covering more surface area than the entire bottom endwall section in the measurement passages, is thermally insulated on the plenum side. This insulation minimizes

**Table 2.** Reference flow-parameters ($2.5C_{ax}$ upstream of cascade and exit plane).

| | |
|---|---|
| Freestream velocity, U | 10.0 m/s |
| Static pressure, $P_{s,r}$ (negative gage) | 60 kPa |
| Velocity boundary layer, δ/S | 10% |
| Temperature boundary layer, $\delta_T$/S | 8% |
| Streamwise turbulence intensity | 3% |
| Integral length-scale of turbulence | 2.3d* |
| Temperature ($T_r$), density ($\rho_r$) | 298 K, 1.02 kg/m$^3$ |
| Coolant to reference: ($\rho_{c,b}/\rho_r$) | 1.0 |
| Coolant to reference: ($T_{c,b}/T_r$) | 1.0-0.94 |
| Reynolds number | 2.0E + 05 |
| based on inlet velocity, $Re_{,r}$ | 6.6E + 05 |
| based on exit velocity, $Re_{,exit}$ | |
| Mach number at exit, $Mach_{,exit}$ | 0.11 |
| Minimum average wall heat-flux | 1000 W/m$^2$ |

*d: rod-diameter of turbulence grid.

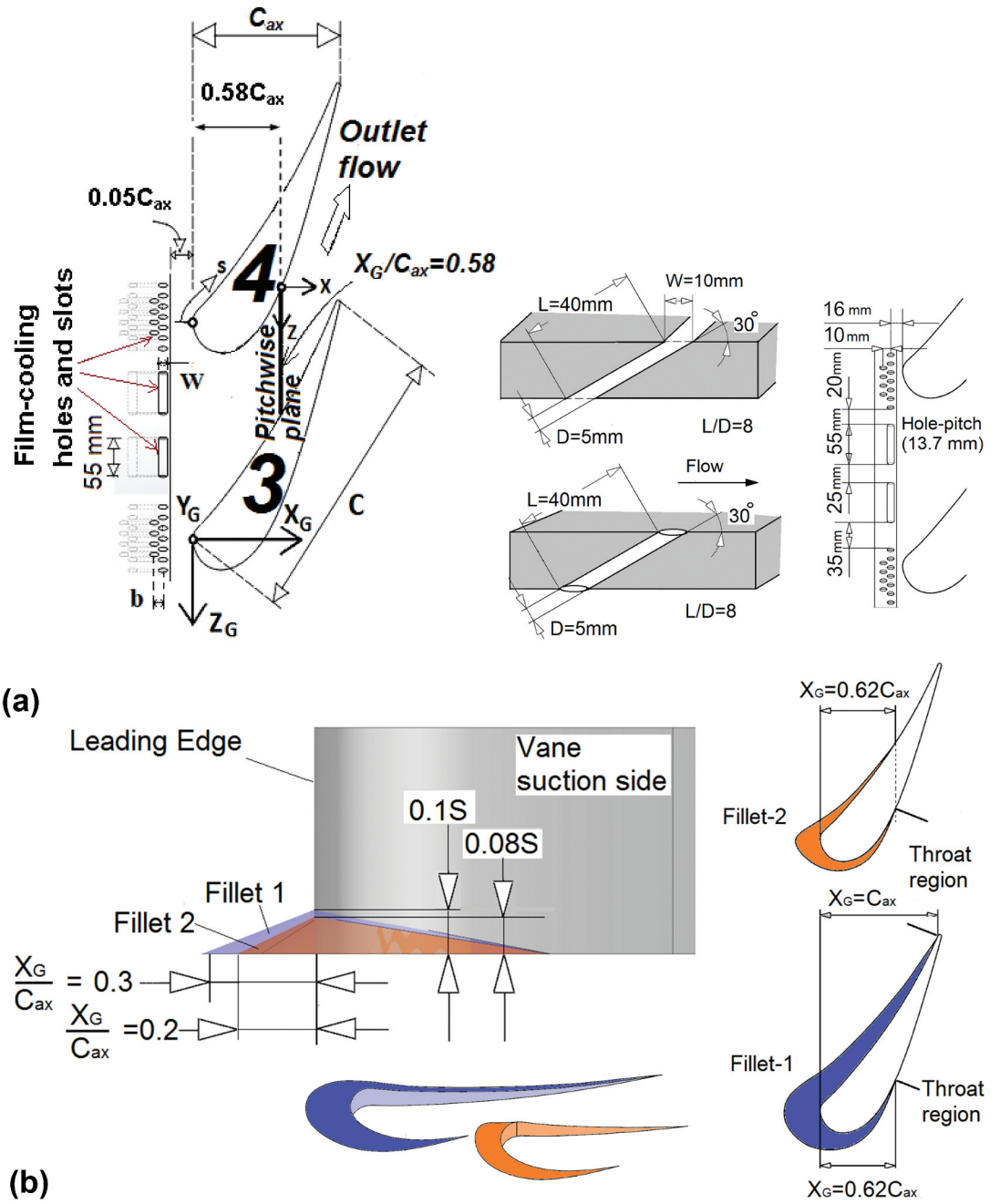


**Figure 2.** (a) Locations and configurations of the slot and straight holes in endwall for film-cooling between vanes-3 and 4 with coordinate systems and flow measurement plane; (b) two fillet profiles.

conduction between the mainstream and plenum fluid during film-cooling effectiveness measurements. Multiple pressure taps have been installed on the walls of the plenum box to measure static and, as a result, total pressure within the system. The local blowing ratio for each hole and slot cannot be regulated due to the use of a singular coolant plenum chamber. The coolant-to-mainstream-flow density ratio is maintained at 1.0. The overall inlet blowing ratio of the film-cooling flow is computed from Eq. (1).

$$M = \left(\frac{P_{t,b} - P_{s,r}}{P_{t,r} - P_{s,r}}\right)^{\frac{1}{2}} \quad (1)$$

Table 3 provides the overall mass fraction ratio (*MFR*) of the coolant to mainstream flow in one passage. The passage mass flow rate, $M_a$ to determine the *MFR* is obtained from the expression of ($\rho_r$, *U,P,S*).

Figure 2(a) illustrates the geometries, positions, and arrangements of the film-cooling discrete slots and cylindrical holes in the endwall, located just upstream of the cascade. The holes are arranged in two rows at the streamwise distance $b = 10$ mm in the leading-edge region, while the two discrete slots are positioned at the pitchwise middle. Both the slot width ($D = 5$ mm) and orientation angle (30°) relative to the endwall surface match the hole diameter ($D$) and orientation. The downstream edges of the slot openings and second-row hole openings are situated 0.05 chord lengths upstream of the vane leading edge. The hole pitch-to-diameter ratio is 2.7, and the length-to-diameter ratio ($L/D$) is 8. These film-cooling hole arrangements align with commonly employed configurations in previous studies (Refs. [14–16]).

Figure 2(a) illustrates the pitchwise measurement plane's position within the cascade and the utilized coordinate systems for data collection. The specified measurement plane, denoted as $X_G/C_{ax} = 0.58$, is positioned 3 mm from the vane surface and 2 mm from the endwall, downstream from the regions where the endwall boundary-layer separates, as referenced in [25]. The coordinate denoted as ($Y_G$ or y) = 0 corresponds to the bottom endwall, while the coordinate "s," which traces along the vane profile, begins at the leading-edge. The cascade's blockage ratio is established at 20%.

Figure 2(b) details the contours and dimensions of two distinct fillets, labeled Fillet-1 and Fillet-2. Both fillets' profiles on the endwall are designed to mirror the vane profile closely. Fillet-1 reaches from the leading-edge to the throat region on both sides of the vane, leaving the passage throat region unaffected by either fillet. Conversely, Fillet-2 spans from the leading-edge to an axial point marked as $X_G = 0.62C_{ax}$ on both the pressure and suction sides of the vane. The design of these fillet geometries is not optimized for peak aerothermal performance; rather, their purpose is to explore the impact on film cooling. The fillet surface height tapers linearly from the vane wall to the endwall and diminishes along the vane profile from the leading-edge, ensuring a seamless integration with the vane wall and endwall at the fillet's trailing end. Fillet-1 and Fillet-2 exhibit variations in maximum height and endwall extension at the leading-edge, as depicted in Figure 2(b). The fillets are substantially larger near the leading-edge to influence the endwall's secondary flows, as indicated in references [3, 7, 8]. These fillets are produced using a three-dimensional printer with commercial plastic filament and subsequently undergo chemical treatment to achieve a smooth finish. The asymmetric three-dimensional form of the fillet, with its height varying from the leading to the trailing side, is conceptualized based on the guidelines in references [3, 26, 27]. Figure 3 presents the examination of five distinct film-cooling configurations, both incorporating and excluding fillets. Accompanying the visual, a table delineates these configurations. The "Reference figure" column in the table aligns with the illustrations (a), (b), (c), and (d) situated above the table. The initial trio of configurations, termed baseline cases within the table, are evaluated without fillets and are distinguished by the variation in blocked film-cooling holes at the leading-edge of the vane. It's important to note that Figure 3(a) depicts the first two baseline scenarios listed in the table, both categorized as case (a).

**Table 3.** MFR (Mc/Ma) of coolant to passage flow.

| M | 2.8 | 2.2 | 1.8 | 1.4 | 1.0 |
|---|---|---|---|---|---|
| Baseline | 0.071369 | 0.067222 | 0.047921 | 0.019729 | 0.005633 |
| Baseline-1 | 0.056730 | 0.053786 | 0.035609 | 0.018942 | 0.004928 |
| Baseline-2 | 0.060062 | 0.057642 | 0.043843 | 0.019312 | 0.005201 |
| Fillet-1 | 0.057508 | 0.058587 | 0.043540 | 0.018527 | 0.004933 |
| Fillet-2 | 0.060781 | 0.058932 | 0.043725 | 0.018941 | 0.005020 |

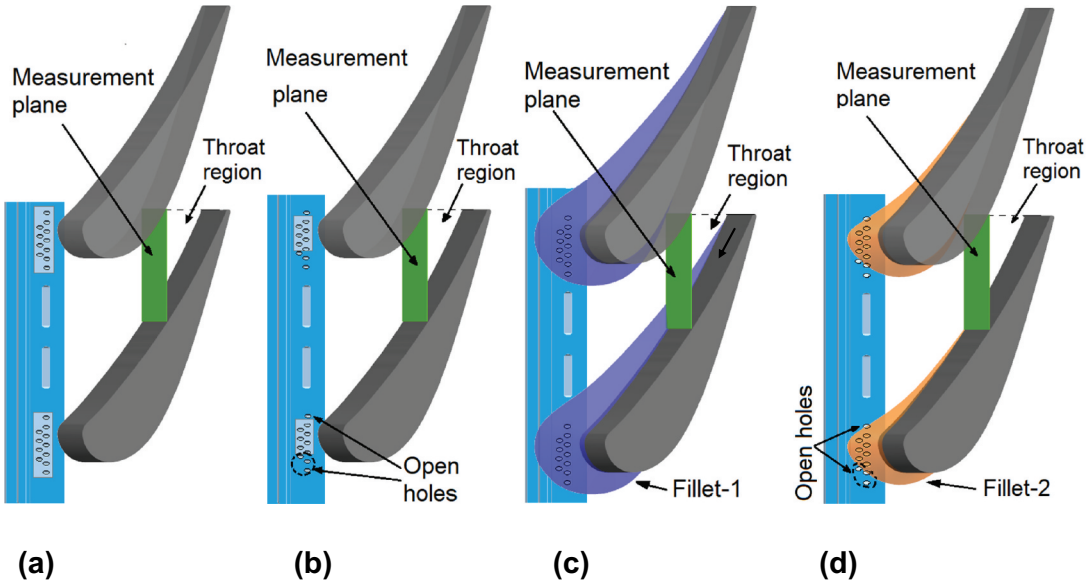


| Reference figure | Film-cooling cases | Configurations |
|---|---|---|
| (a) | Baseline | Film-cooling slots and all holes open, no fillet |
| (a) | Baseline-1 | Film-cooling slots open and all holes closed, no fillet |
| (b) | Baseline-2 | Film-cooling slots and marked holes open, no fillet |
| (c) | Fillet-1 | Film-cooling slots open and all holes closed, Fillet-1 |
| (d) | Fillet-2 | Film-cooling slots and marked holes open, Fillet-2 |

**Figure 3.** Five film-cooling configurations in endwall relative to the fillet profiles: (a) Baseline and baseline-1, (b) baseline-2, (c) fillet-1, (d) fillet-2.

The custom-built thermal probe, equipped with a K-type thermocouple, features a 10 mm tip. This tip houses a 0.4 mm diameter thermocouple junction nestled between two prongs at the end of a lengthy metal stem. Following calibration, the probe is inserted into the top endwall through a designated slot at the measurement plane's location. Pressure measurement employs a commercial five-hole pressure probe featuring a 2.5 mm a cobra conical tip diameter. All probe tips are aligned with the mid-span, streamwise direction of the freestream, both upstream and within the cascade. Probe traversal is conducted along the reference and measurement planes using a two-axis motorized system, with spatial resolutions of 2.0 mm adjacent to walls and 5.0 mm elsewhere. Each traversing pressure probe port connects to a differential pressure transducer, utilizing two for the pitot-static pressure probe and five for the five-hole pressure probe, to capture pressure data. Wall static pressure ports are linked to a single differential pressure transducer through a manual scanner. Detailed information on the flow measurement setup can be found in Arnachellan [24]. Data acquisition occurs at rates of 100 hz for 2 s for pressure, 60 hz for 2 s for temperature, and 5 kHz for 10 s for turbulence intensity, all recorded via National Instruments™ data-logger cards NI PXIe01062Q. Nine Omega transducers were used to measure the pressure variation. A singular Labview™ program manages data capture and traverse motion. Voltage readings from the data-logger cards are averaged over time and converted to flow property units using the relevant calibration curves. Calibration adjustments

for spatial dimensions and streamline curvature specific to the five-hole pressure probe are detailed in Ref [24].

In the study, the endwall's heat transfer and film-cooling effectiveness are gauged through infra-red thermal imaging. This method captures the thermal footprint of the endwall, which is either heated or cooled, using a high-resolution infra-red video camera FLIR A35sc. The camera, which boasts a resolution of $320 \times 256$ pixels and a 16-bit pixel depth, records the endwall's thermal state through a Zinc-Selenide window. It operates at a 60 hz frame rate with an emissivity setting optimized to 0.96. To ensure maximum emissivity and minimal reflection, the endwall is coated in black paint.

The top endwall features four strategically placed windows (Figure 1), enabling comprehensive coverage of the area between vanes 3 and 4, as indicated in Figure 1. Images captured over a 20-s duration at each window are averaged to mitigate transient effects. These pixel values are then translated into temperature readings in degrees Celsius, utilizing a specialized image-processing program and the camera's built-in calibration functions. Subsequently, the individual images from all windows are amalgamated to form a complete thermal map of the endwall.

To convert the pixel-based temperature data into accurate surface temperature readings, an in-situ calibration method, as outlined by Sargent et al. [28], is employed. This involves the placement of 45 calibrated thermocouple tips across the endwall, inserted through pre-drilled holes to sit flush with the surface on the measurement side. The space around the thermocouple wires is sealed with thermally conductive paste to ensure precise temperature readings. This meticulous process allows for the accurate interpretation of the thermal images, providing valuable insights into the endwall's thermal characteristics under various cooling conditions.

Figure 4 displays calibration results for pixel temperatures on thermal images, corresponding to surface thermocouple points. The figure features two calibration datasets, both derived from the same viewing window. The initial dataset, ranging from 35°C to 75°C, is captured during a heated-wall Nusselt number evaluation without the fillet. The subsequent dataset, spanning 8°C to 18°C, is recorded during an adiabatic film-cooling effectiveness assessment at $M = 2.8$, also without the fillet. Each thermal image from a viewing window includes a minimum of 10 calibration points. These points are analyzed using a least squares-fit linear regression to translate pixel values into actual surface temperatures. The regression's correlation coefficient consistently exceeds 0.97 indicating that the thermocouple readings are reliable and consistent. A correlation coefficient exceeding 0.97 indicates an extremely strong positive linear relationship between pixel temperature to wall temperatures ($T_w$) which reflect the uniformity of the heat flux over the endwall. This also shows that the readings from the thermocouple points on the endwall is perfectly consistent which a strong indication of constant heat flux on the enwall. For every test scenario, a unique calibration equation correlates pixel temperature to wall temperatures ($T_w$) for each averaged image from a window. The in-situ calibration process, as depicted in Figure 4, is conducted under real measurement conditions, ensuring that the pixel temperature adjustments reflect any heat conduction through the endwall.

For the purpose of measuring heat transfer coefficients in presence of no film cooling, a 0.3 mm thick foil heater is affixed to the bottom endwall on the flow side as shown in Figure 1. This heater consists of copper tape strips, each 6 mm in width and 0.10 mm in thickness, layered between two Kapton™ foils and arranged parallelly with a gap of approximately 0.1 mm. The copper strips are soldered into a serpentine configuration to form a continuous resistive heating element, tailored to fit the pitchwise length of the cascade's measurement passages. Due to the unique shape of the cascade passage, standard commercial foil heaters were not compatible, and thus, a custom foil heater was fabricated. However, this custom heater does not extend over the fillet surface due to its complex three-dimensional shape and integration with the vane and endwall toward the trailing edge. The vane surface itself is not equipped with a heater and is presumed to be adiabatic for the purposes of endwall heat transfer analysis.

The endwall heating commences approximately $3.5C_{ax}$ upstream from the cascade inlet and is powered by a DC power supply. The copper strips' consistent thickness, width, and resistivity ensure a steady current density and uniform heat flux across the heater. For infra-red thermal

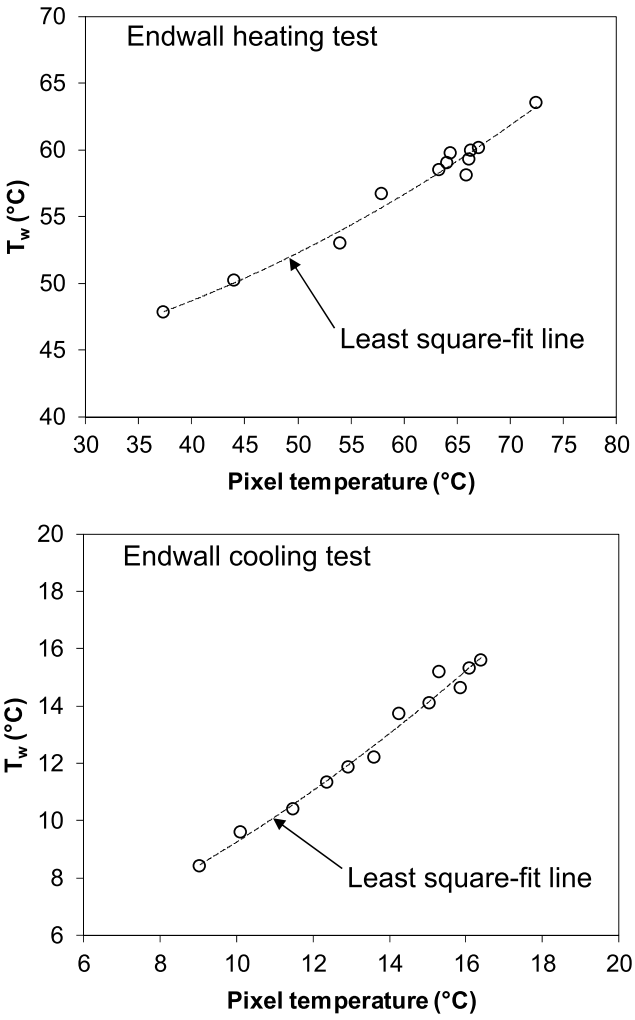


**Figure 4.** Sample of in-situ calibrations of thermal image-pixels with wall temperatures ($T_w$) at the thermocouple locations during heating and cooling of endwall without the fillet.

imaging, the heater's flow side is coated in black paint. Thermocouple tips, penetrating through the endwall, make direct contact with the heater's surface. The convective heat transfer, denoted as $Q_{conv}$, to the passage flow is calculated using Eq. (2), while the conductive heat loss, $Q_{cond}$, through the endwall is determined through one-dimensional conduction analysis, considering the temperature differential between the heater's surface and the insulated side of the endwall. The conductive heat loss constitutes a mere 1% of the electrical power supplied to the heater, $P_{heater}$.

The average wall heat flux, represented as $Q_{cond}/\ P_{heater}$, is subsequently utilized in Eq. (3) to ascertain the local Nusselt number, Nu, on the endwall. Table 2 lists the minimum average heat flux values used for the heat transfer measurements. Air properties such as thermal conductivity ($k_{air}$) and viscosity ($\mu$) are derived from the reference flow pressure and temperature. The local wall temperature, $T_w$, required for Eq. (3) and Eq. (4) is obtained from the in-situ calibration of the pixel temperature of the thermal image. The adiabatic film-cooling effectiveness, $\eta$ on the endwall is estimated from Eq. (4).

$$Q_{\text{conv}} = P_{\text{heater}} - Q_{\text{cond}} \tag{2}$$

$$Nu = \frac{(Q_{conv}C)}{A_{heater}(T_w - T_r)k_{air}} \tag{3}$$

$$\eta = \frac{(T_r - T_w)}{(T_r - T_{c,b})} \tag{4}$$

The assessment of errors in both the measured and computed values adheres to the 95% confidence interval and error propagation methods detailed in references [29, 30]. Uncertainties for velocity and pressure measurements are pegged at 1.6% and 3.6%, respectively. The static-pressure coefficient and total-pressure loss coefficient are subject to uncertainties up to 5.7% and 8.2%, respectively. The film-cooling flow rate's maximum uncertainty stands at 0.7%, while the inlet blowing ratio's uncertainty reaches 1.4%. Temperature readings from thermocouples and wall heat-flux calculations carry an uncertainty of 4.0%. Consequently, thermal image data is associated with a temperature uncertainty of 6.1%, a Nusselt number uncertainty of 8.2%, and the averaged adiabatic effectiveness uncertainty of 10%.

## Discussions of results

Measurements were conducted under quasi steady-state conditions, with pressure and temperature variations within the test section maintained below ±2 Pa (gage) and ± 0.2°C, respectively, over a span of 10 min. Variations in reference velocity, static pressure, and temperature were limited to a maximum of 0.2 m/s, 0.5 kPa (gage), and 0.2°C, respectively, across different test scenarios. For flow measurements, the ratio of coolant to reference temperature (absolute), $T_{c,b}/T_r$, was set at 1.0, and 0.94 for measuring adiabatic wall temperature during film-cooling effectiveness tests. Both the walls and fillets were considered adiabatic for these flow measurements. Results are showcased for the passage between vanes 3 and 4, as depicted in Figure 1, with fillets implemented on the bottom endwall.

Fillets and film-cooling techniques were applied to the bottom endwall in the passages between vanes 3, 4, and 5. The flow field characteristics of the cascade without film-cooling and fillets have been previously detailed in [4] and are not reiterated here, as the current focus is on examining the impact of fillets on endwall heat transfer and film-cooling. It is important to note that the film- cooling configurations, including the discrete holes in the current baseline, Baseline-2, and Fillet 2 cases, differ from those presented in [4, 5].

### *Inlet flow: boundary layer and turbulence*

Figure 5 delineates the inlet flow's velocity and temperature profiles across the channel height, denoted as $Y_G/S$. Due to the size of the probes, measurements in proximity to the endwall ($Y_G/S = 0$) are not feasible. However, further from the endwall, both velocity and temperature closely align with the freestream values, $U$ and $T_r$, reaching 99% at approximately $Y_G/S \approx 0.1$ and $Y_G/S \approx 0.08$, respectively. The turbulence intensity, calculated at 3% relative to $U$ and listed in Table 2, is derived from the $X_G$-component velocity fluctuations captured by the X-wire probe of a hot-wire anemometer. While detailed statistical turbulence data wasn't recorded for length-scale analysis, the observed intensity aligns well with predictions by Roach [31]. Utilizing Roach's correlations for a parallel-rod grid, the freestream's turbulence length-scale (integral) is estimated in Table 2. At the cascade inlet, the turbulence intensity and length-scale (integral) are anticipated to be around 1.6% and 3$d$, respectively, as per Ref [31]. The upstream passive turbulence grid's geometry was chosen to minimize turbulence and flow blockage, achieving a high Reynolds number ($Re$) of 2.0E + 05 at the cascade inlet.

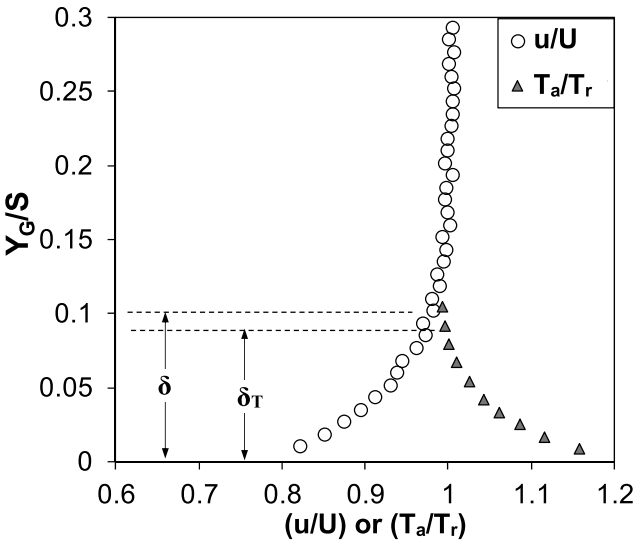


**Figure 5.** Inlet flow velocity (u/u) and temperature ($T_a/T_r$) profiles along cascade span, $Y_G/S$ in reference plane $2.5C_{ax}$ upstream of cascade inlet. Temperature profile is obtained with heated endwall.

Conducting film-cooling studies in vane cascades under low turbulence intensity (<1.5%) is a standard practice in the field, as referenced in the literature [10, 11, 13, 15, 18–20].

## *Cascade flow periodicity*

The measurements were conducted under periodic flow conditions within the cascade to emulate a turbine vane row. The pressure coefficient, ($C_{p,b}$), profiles depicted in Figure 6 for vanes 3, 4, and 5 at mid-span height are instrumental in ensuring these conditions. In the figure, the vane-profile coordinate, ($s/C = 0$), marks the leading-edge; ($s/C > 0$) corresponds to the pressure side (PS), and ($s/C < 0$) to the suction side (SS). Wall pressures, ($P_b$), recorded along the vane profiles, feed into Eq (5) to calculate ($C_{p,b}$).

$$C_{p,b} = \frac{(P_b - P_{s,r})}{(P_{t,r} - P_{s,r})} \tag{5}$$

Figure 6 compares ($C_{p,b}$) values with and without fillets, in scenarios where film-cooling flow is not introduced ($M = 0.0$). The negative ($C_{p,b}$) values beyond the leading-edge area reflect the pressure reduction along the vane surface, indicating ($P_{s,r} > P_b$). The consistency of ($C_{p,b}$) distributions across the plots for each vane suggests a balanced mass flow through the passages.

## *Total pressure loss*

Figure 7 illustrates the distribution of the total pressure loss coefficient, $C_{pt,loss}$, for both the baseline and filleted configurations without film-cooling flow ($M = 0.0$) across the pitchwise plane at $X_G/C_{ax} = 0.58$. The $C_{pt,loss}$ values, derived from the total pressures measured, Pt, in the plane using Eq (5), are notably elevated in the secondary flow region, demarcated by $0 < Z/P < .35$ and $0 < Y/S < 0.15$ near the suction side (SS). This region is characterized by significant total pressure losses, expressed as ($P_{t,r}$ - $P_t$). In Figure 7, areas with $C_{pt,loss}$ values of 0.8 or higher, particularly in the left-hand corner at the SS, delineate the magnitude and intensity of the passage vortex core. The region with the most substantial pressure loss is found where $Y/S < 0.20$, coinciding with the convergence of the passage vortex and the suction-side leg vortex near the SS and just before the passage throat, as cited in references [27, 32–34].

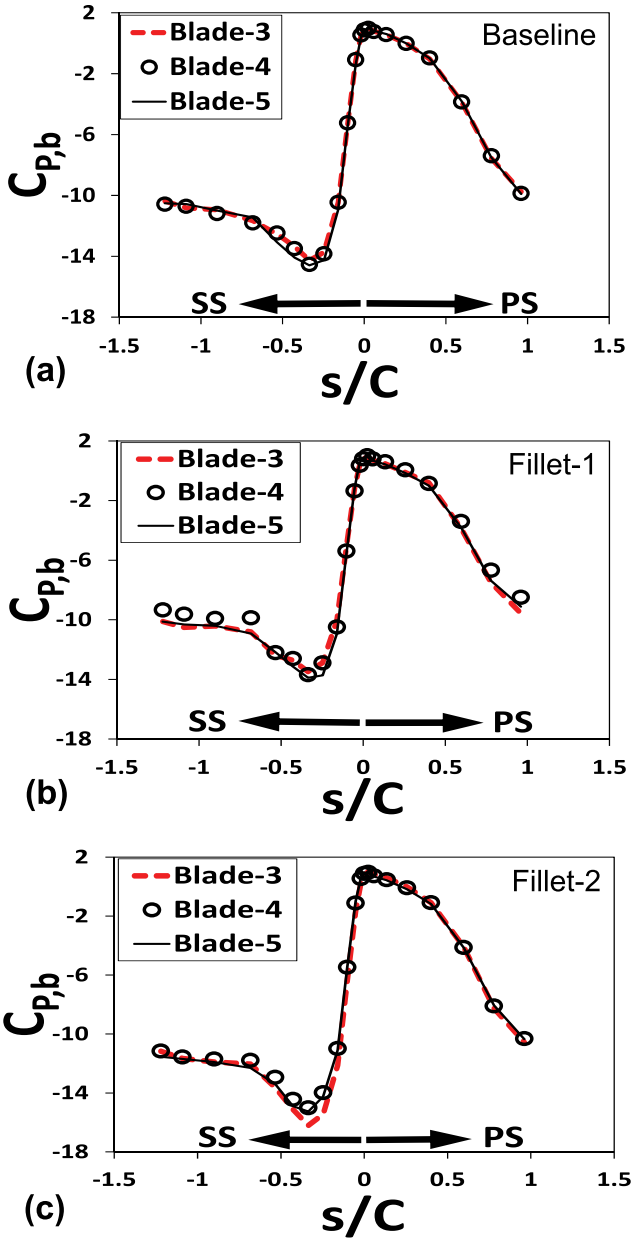


**Figure 6.** Surface pressure coefficients, $C_{p,b}$ along profiles of vanes-(3, 4, 5) at Y/S = 0.5 with $M = 0.0$: (a) baseline without fillet, (b) fillet-1, (c) fillet-2.

The contour area with $C_{pt,loss}$ values of 0.8 or greater indicates that the passage vortex core is most pronounced and potent in the baseline case, and notably less so in the Fillet-2 case. For the Fillet-1, the presence of a $C_{pt,loss}$ contour of 1.8 at the SS corner in Figure 7(b) suggests that the passage vortex core is slightly raised from the endwall compared to the baseline. The heightened $C_{pt,loss}$ values near the SS, specifically at Z/P < .03 for the Fillet-2, result from increased ($P_{t,r}$ - $P_t$) values due to flow obstruction between the measuring probe-stem and the vane wall. The absence of contours in the lower right-hand corner of Figure 7(b) is attributed to the volume of the Fillet-1. The influence of the diminished passage vortex on the endwall Nu distributions has been previously established in Figure 7.

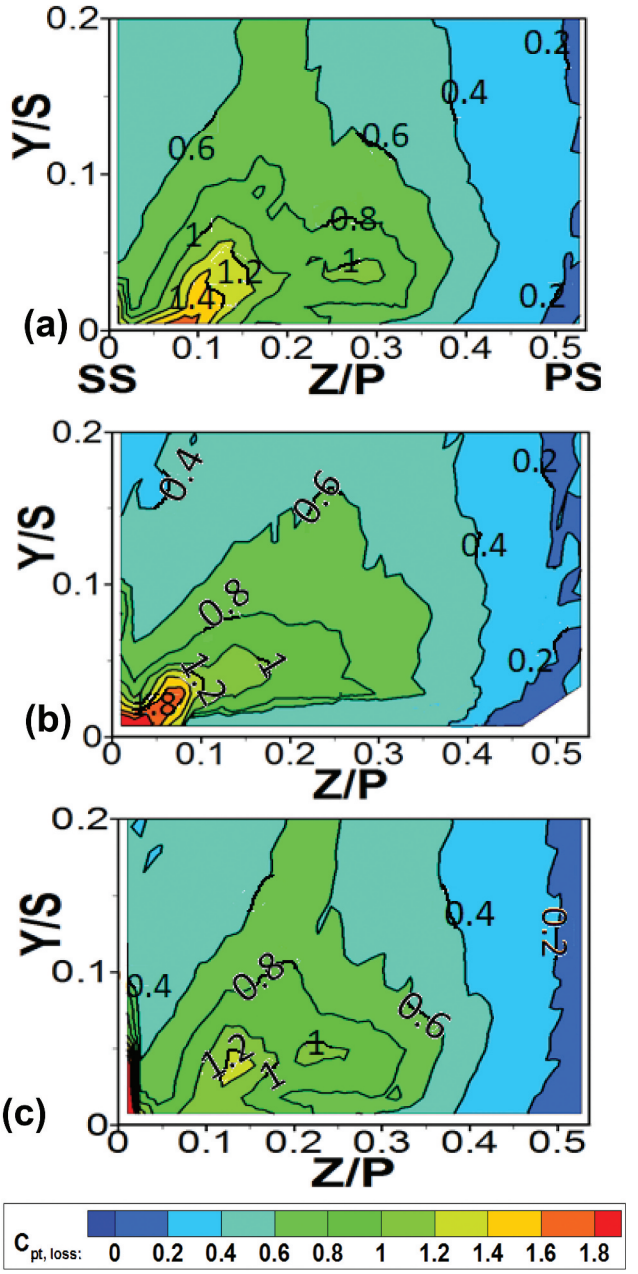


**Figure 7.** Total pressure loss coefficient, $C_{pt,loss}$ contours in pitch-plane at $X_G/C_{ax} = 0.58$ when $M = 0.0$ for: (a) baseline, (b) fillet-1, and (c) fillet-2.

$$C_{pt,loss} = \frac{(P_{t,r} - P_t)}{(P_{t,r} - P_{s,r})} \tag{6}$$

Figures 8–10 display the $C_{pt,loss}$ distributions in the pitchwise plane at $X_G/C_{ax} = 0.58$, incorporating film-cooling ($M > 0.0$). These figures highlight the passage-vortex core's location, dimensions, and intensity, and also shed light on the penetration and interaction of the coolant near the endwall. The impact of the coolant flow on the endwall's secondary flows is evident. Nonetheless, discerning the

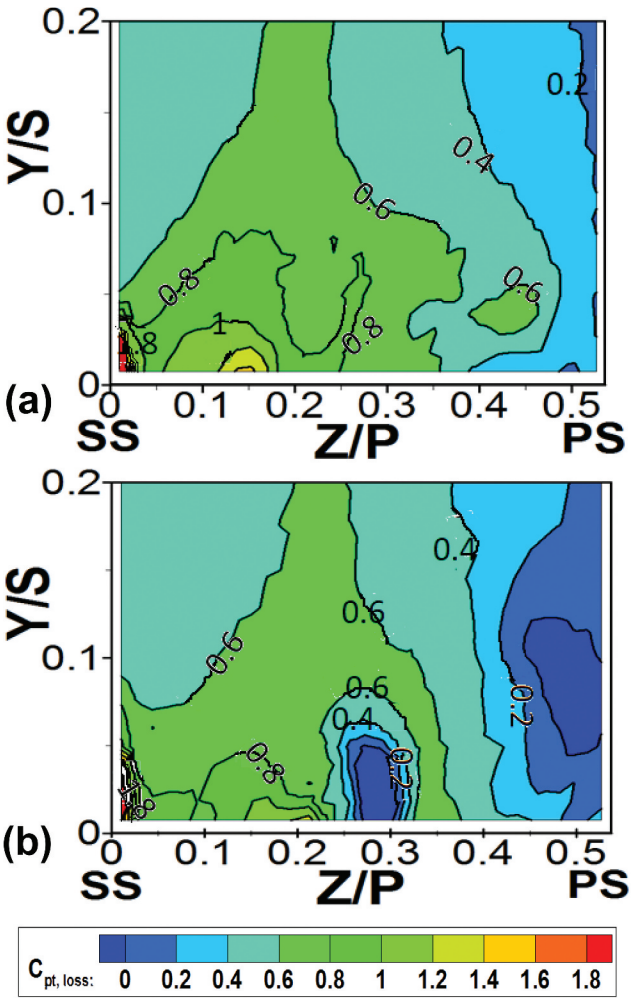


**Figure 8.** Total pressure loss coefficient, $C_{pt,loss}$ contours in pitch-plane at $X_G/C_{ax} = 0.58$ for the baseline when: (a) $M = 1.4$ and (b) $M = 2.2$.

influence of the endwall's secondary flows on the film-cooling flow patterns from the local $C_{pt,loss}$ is challenging. Due to the probe's size causing flow obstructions and altering streamlines, flow data cannot be collected in close proximity to the walls. The clusters of $C_{pt,loss} \geq 0.8$ contours above the endwall at $Z/P < .33$ stem from the passage vortex and its interaction with the coolant flow and boundary layer. When film-cooling is applied, the passage-vortex core, marked by the highest contour values, shifts away from the SS corner, unlike in non-cooled scenarios. Shote et al. [20] demonstrate that the coolant flow, elevated by the passage vortex legs, mingles with the vortex structures, altering the $C_{pt,loss}$ distribution within the vortex core. Conversely, Mahmood and Arnachellan [18, 19] observe a reduction in local $C_{pt,loss}$ values within the passage vortex for slot film-cooling scenarios. The coolant flow's penetration into the boundary layer above the endwall diminishes $C_{pt,loss}$ values, as the coolant streams' robust jet momentums lessen the pressure losses, denoted by $(P_{t,r} - P_t)$. The coolant flow from the three open-holes at the fillet-2 edge pushes up the suction side-leg vortex. At location $X_G/C_{ax} = 0.58$, the interactions of the suction side-leg vortex with the passage vortex, endwall boundary layer, and lifted coolant flow cause the region of concentrated high $C_{pt,loss} > 1.4$ above the endwall and adjacent to the suction side in Figure 9(d). The effects of the interactions are enhanced as some coolant flow penetrates into the endwall boundary layer at the high blowing ratio of $M = 2.2$. The region of

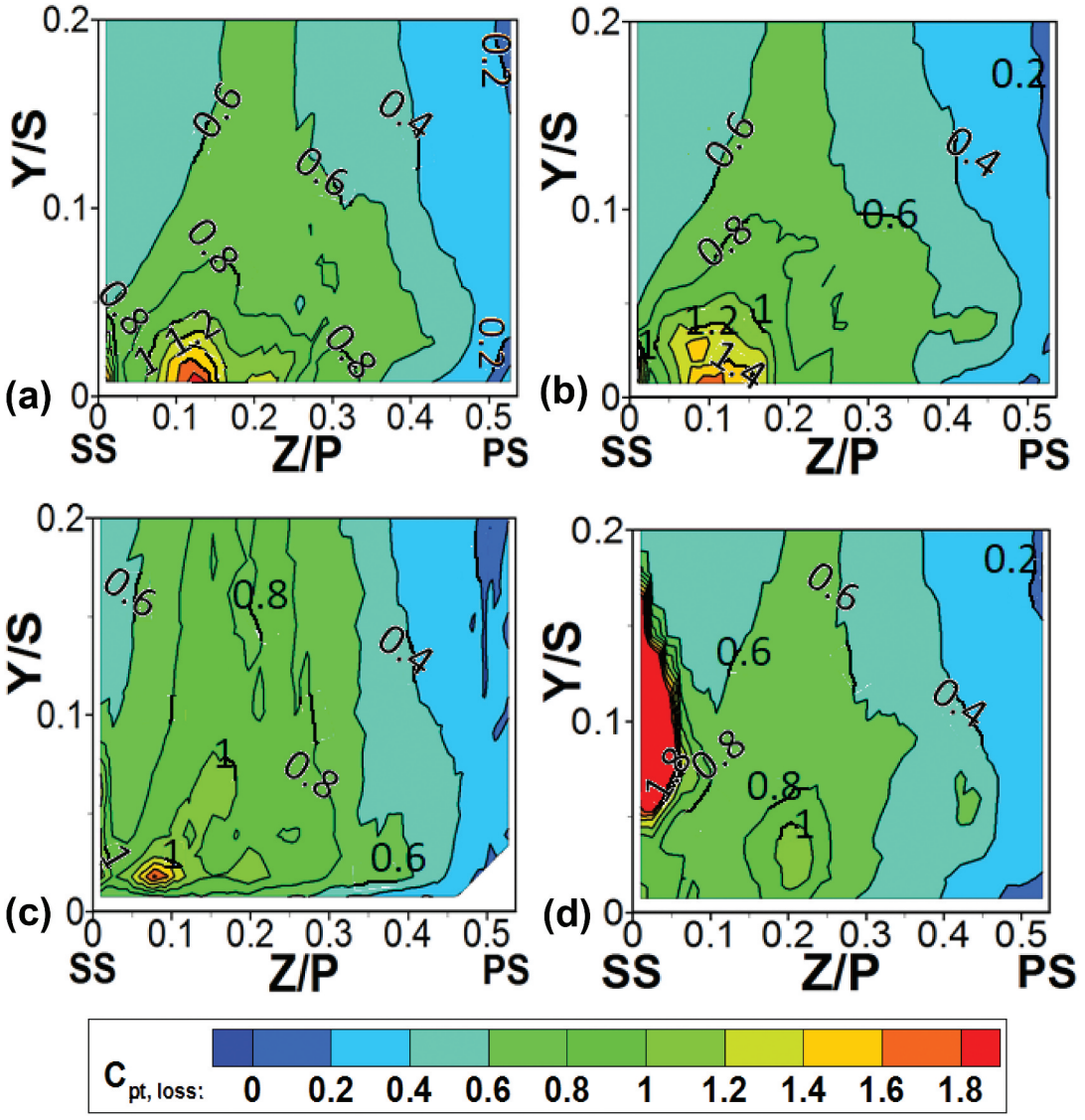


**Figure 9.** Total pressure loss coefficient, $C_{pt,loss}$ contours in pitch-plane at $X_G/C_{ax} = 0.58$ when $M = 1.4$ for: (a) Baseline-1, (b) baseline-2, (c) fillet-1, and (d) fillet-2.

concentrated $C_{pt,loss}$ >1.4 adjacent to the suction side is then larger and located higher above the endwall in Figure 10(d). In Figures 8 to 10, areas with $C_{pt,los}$ <0.2 near the pressure-side (PS) and just over the endwall result from the coolant's liftoff. The coolant's elevated penetration above the endwall decreases its coverage and, consequently, the film-cooling efficacy on the endwall.

The comparison between the baseline scenarios depicted in Figure 8 (with blowing ratios $M = 1.4$ and 2.2) and Figure 7(a) ($M = 0.0$) reveals that the $C_{pt,loss}$ values within the passage vortex core near the SS corner are reduced in Figure 8. Specifically, a higher blowing ratio of $M = 2.2$ in Figure 8(b) further diminishes the $C_{pt,loss}$ values, consequently shrinking the passage vortex size. Notably, the presence of $C_{pt,loss}$ values equal to or less than 0.0 in Figure 8(b) for $M = 2.2$ signifies the elevated momentum of coolant-jets detaching from the endwall.

Figures 9 and 10 delineate the $C_{pt,loss}$ for $M = 1.4$ and $M = 2.2$ across various cases including Baseline-1, Baseline-2, Fillet-1, and Fillet-2. In Figure 9(c), the Fillet-1 scenario exhibits a smaller

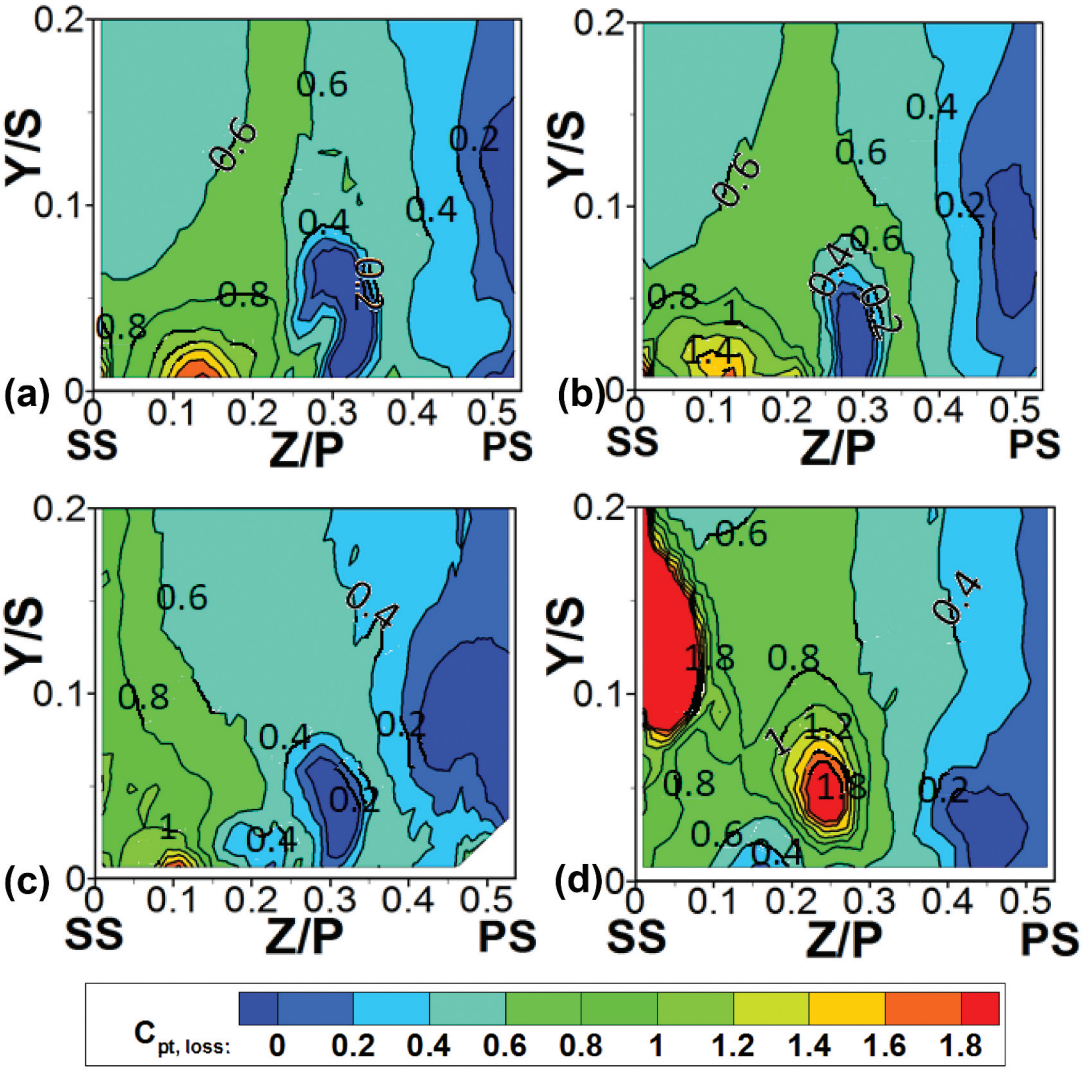


**Figure 10.** Total pressure loss coefficient, $C_{pt,loss}$ contours in pitch-plane at $X_G/C_{ax} = 0.58$ when $M = 2.2$ for: (a) Baseline-1, (b) baseline-2, (c) fillet-1, and (d) fillet-2.

passage-vortex core with $C_{pt,loss}$ ≥0.8 near the SS corner compared to the baseline cases shown in Figure 9(a, b). For Fillet-2, as shown in Figure 9(d), the area with higher $C_{pt,loss}$ ≥1.8 adjacent to the SS is attributed to the amalgamation of the ascending coolant flow with the passage vortex and boundary layer. This area is slightly more pronounced and raised in Figure 10(d) with a higher $M = 2.2$. The elevated coolant flows contributing to the $C_{pt,loss}$ ≥1.8 region primarily originate from discrete holes at the edge of Fillet-2, as referenced in Figure 3. For the Baseline and Baseline 2 cases, the coolant flows from the leading-edge (LE) discrete holes are uplifted and redirected by the suction-side leg vortex, resulting in the absence of $C_{pt,loss}$ ≥1.8 regions adjacent to the SS in Figures 8, 9(b), and 10(b).

With an increase in the blowing ratio to $M = 2.2$ in Figure 10, the area indicating the passage-vortex core size, marked by $C_{pt,loss}$ ≥0.8, is significantly altered for all cases. The $C_{pt,loss}$ ≥1.0 region of the passage-vortex core in Figure 10(a, b, c) is now more compact compared to the analogous scenarios in Figure 9(a, b, c) with $M = 1.4$. The $C_{pt,loss}$ ≥1.0 zone between $0.2 < Z/P < .3$ for Fillet-2 in Figures 9(d) and 10(d) results from the mixing losses of the film-cooling flow with the boundary layer. The $C_{pt,loss}$

≥1.0 area adjacent to the endwall appears marginally larger for Baseline-2 than for Baseline-1 in Figures 9(a,b) and 10(a,b). Moreover, the Cpt,loss ≥1.0 region near the SS is more extensive and elevated for Fillet-2 compared to Fillet-1 in Figures 9(c,d) and 13(c, d).

The analysis of the $C_{pt,loss}$ ≤0.0 region in Figure 10 suggests that the Fillet-2 case offers the least penetration of the film-cooling flow into the boundary layer. The film-cooling configurations near the vane's leading-edge region in the filleted cases differ slightly in this study from those in Ref [20]. Consequently, the $C_{pt,loss}$ distributions and the interactions of the film-cooling flow with the boundary layer near the endwall at $M = 1.4$ and 2.2 vary between the two studies.

In Figures 8(a) and 9(a, b), as well as in Figures 8(b) and 10(a, b), the dimensions and positioning of the passage-vortex core with $C_{pt,loss}$ ≥0.8 within the range of $0.05 < Z/P < .25$ are similar for the baseline scenarios. However, within the same $Z/P$ range, the $C_{pt,loss}$ values for the passage-vortex core are lower for the Baseline case compared to Baseline-1 and Baseline-2, both at a mass flow ratio (MFR) of 1.4 in Figures 8(a) and 9(a, b), and at an MFR of 2.2 in Figures 8(b) and 10(a, b). According to Table 3, the baseline's higher coolant mass flux and momentum lead to reduced $C_{pt,loss}$ values within the passage-vortex core. As the MFR increases, so do the coolant mass-flux and momentum, which in turn diminish the intensity of the passage-vortex core. The film-cooling flow emanating from the discrete holes in the leading-edge (LE) endwall region for the baseline case is thus effective in weakening the passage-vortex core. Similarly, the film-cooling flow from the leading-edge slots in the baseline case, as studied in Refs [4, 6], also has a notable impact on the passage vortex.

The studies referenced in [32, 35] suggest that freestream turbulence has a minimal impact on the formation and configuration of the leading-edge horseshoe vortex as well as the secondary flows near the endwall of a vane cascade. The $C_{pt,loss}$ patterns depicted in Figure 7, which lack film cooling, are primarily influenced by the passage vortex and are likely to remain consistent even under conditions of elevated freestream turbulence. Colban et al. [10] and Li et al. [36] have found that, with the introduction of film-cooling from the upstream endwall, the distribution of film-cooling within the cascade passage improves at a specific blowing ratio as the intensity of freestream turbulence rises. The mass flux and momentum of the coolant are proportional to the density ratio ($\rho_{c,b}/\rho_r$) for a given M. An increase in the momentum of the film-cooling jet, due to a higher density ratio ($\rho_{c,b}/\rho_r$) could potentially lower the elevated $C_{pt,loss}$ values observed above the endwall in the current study.

### *Endwall Nusselt number and flow field (M = 0.0)*

In Figure 11, the Nusselt number ($Nu$) distributions illustrate the localized areas of intense heat transfer along the endwall, both with and without fillets, and in the absence of film-cooling flow ($M = 0.0$). The color-coded values of $Nu$ in Figure 11(a–c) are defined in a unified legend located to the right of Figure 11(c). Areas devoid of contour lines represent the profiles of the vane and fillet on the endwall. Since the fillets are not subjected to heating, no heat transfer coefficient data is recorded for their surfaces. Generally, the $Nu$ values escalate from the entry region down the passage in all scenarios depicted in Figure 11(a–c), mirroring the flow acceleration observed in baseline cascade studies without fillets [32, 34, 35, 37, 38]. In the vicinity of the vane's pressure and suction sides, specifically in the range of $0.0 < X_G/C_{ax} < 0.15$, $Nu$ values are elevated due to the influence of the pressure side-leg and suction side-leg vortex legs. However, the three-dimensional separation lines that encircle these vortex legs, which are apparent below $X_G/C_{ax}$ <0.6 as per Huyssen et al. [25], are not discernible in Figure 11(a–c) due to the minimal contrast between high and low $Nu$ levels caused by flow acceleration. These separation lines are also absent in the heat transfer patterns on the cascade endwall reported in references [32, 38]. For the Fillet-2 case within $0.2 < X_G/C_{ax} < 0.6$ in Figure 11(c), the $Nu$ values are notably lower compared to other scenarios. This segment of the endwall is profoundly affected by the passage vortex and its two vortex legs as they progress along the endwall [7, 25, 37]. The diminished $Nu$ values in this region are likely a result of the attenuated vortex legs when Fillet-2 is utilized, aligning with findings from a study on a filleted blade cascade by Mahmood et al. [39]. It is anticipated that local $Nu$ values outside the three-dimensional separation zones, namely beyond the

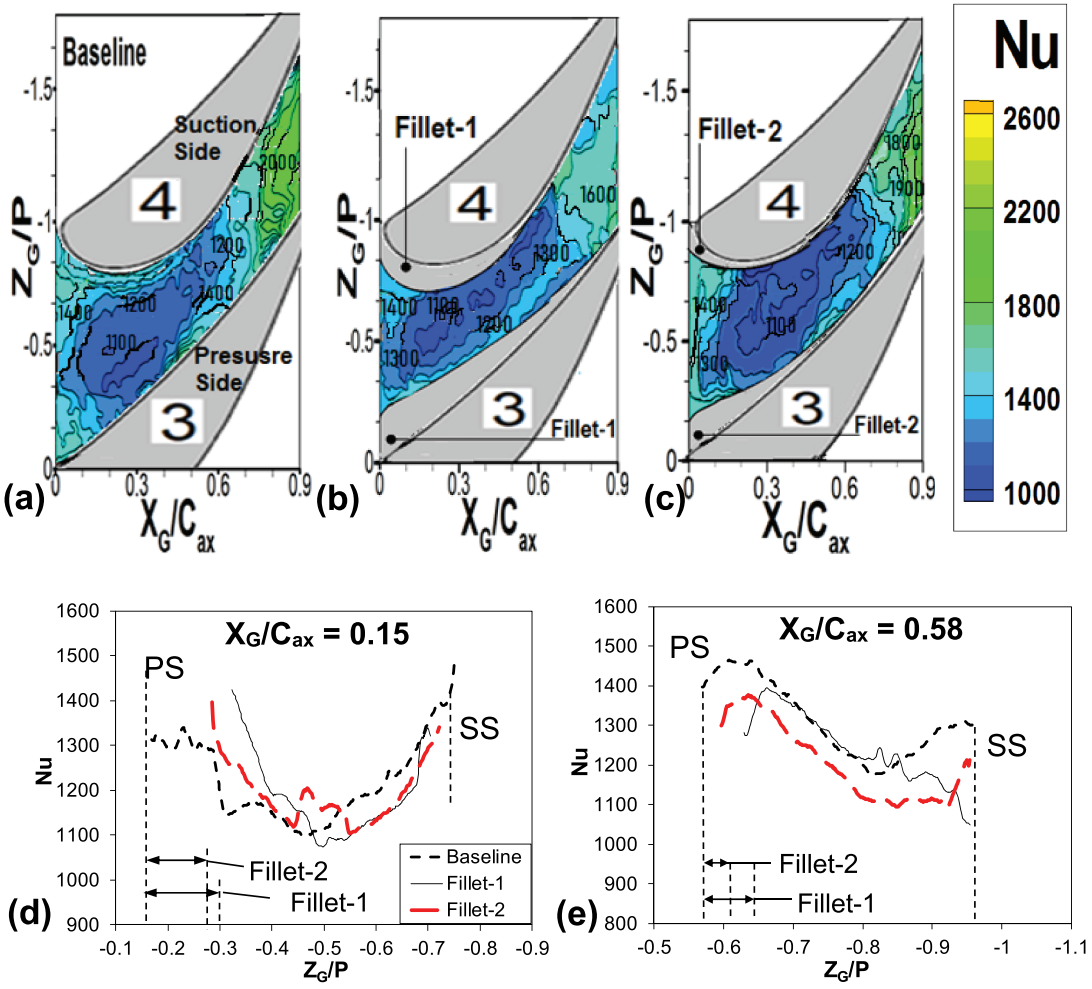


**Figure 11.** Nusselt number (nu) distributions with $M = 0.0$: (a-c) along endwall, (d, e) pitchwise nu at two axial-positions. Contour values for 11(a-c) are shown in on the right side of 11(c). Symbol legends of 11(d, e) are shown in fig. 11(d).

leading-edge (LE) horseshoe vortex and passage-vortex legs, could rise if the freestream turbulence level exceeds 3%, as suggested by the outcomes in references [32, 35].

The increased unsteadiness in the boundary layer flow with the turbulence level will cause the increase in *Nu*. In the three-dimensional separation regions, the heat transfer from the endwall is dominated by the strong vortex motions and *Nu* values will remain about the same as the turbulence increases. Downstream of the throat region the effects of freestream turbulence on the *Nu* will diminish as the flow accelerates reducing the local turbulence significantly. However, the turbulence induced by the large swirling motions in the freestream studied by Werschnik et al. [38] will increase the *Nu* values everywhere along the endwall.

The differences in the *Nu* distributions between the baseline and fillet cases are further illustrated by the *Nu* data along the pitch-lines or $Z_G/P$ locations at two axial-positions of $X_G/C_{ax} = 0.15$ and 0.58 in Figure 11(d, e). Near the pressure side (PS) and suction side (SS), the *Nu* values increase where the local flow (streamwise) accelerations are higher and the influences of passage-vortex legs are significant. The values are generally the smallest for the Fillet-2 at $X_G/C_{ax} = 0.58$.

Figure 12(a) examines the influence of the fillet on the pitchwise pressure gradients, ($P_{s,p}$ - $P_{s,ss}$), which are instrumental in directing the flow towards the suction side and in the formation of the

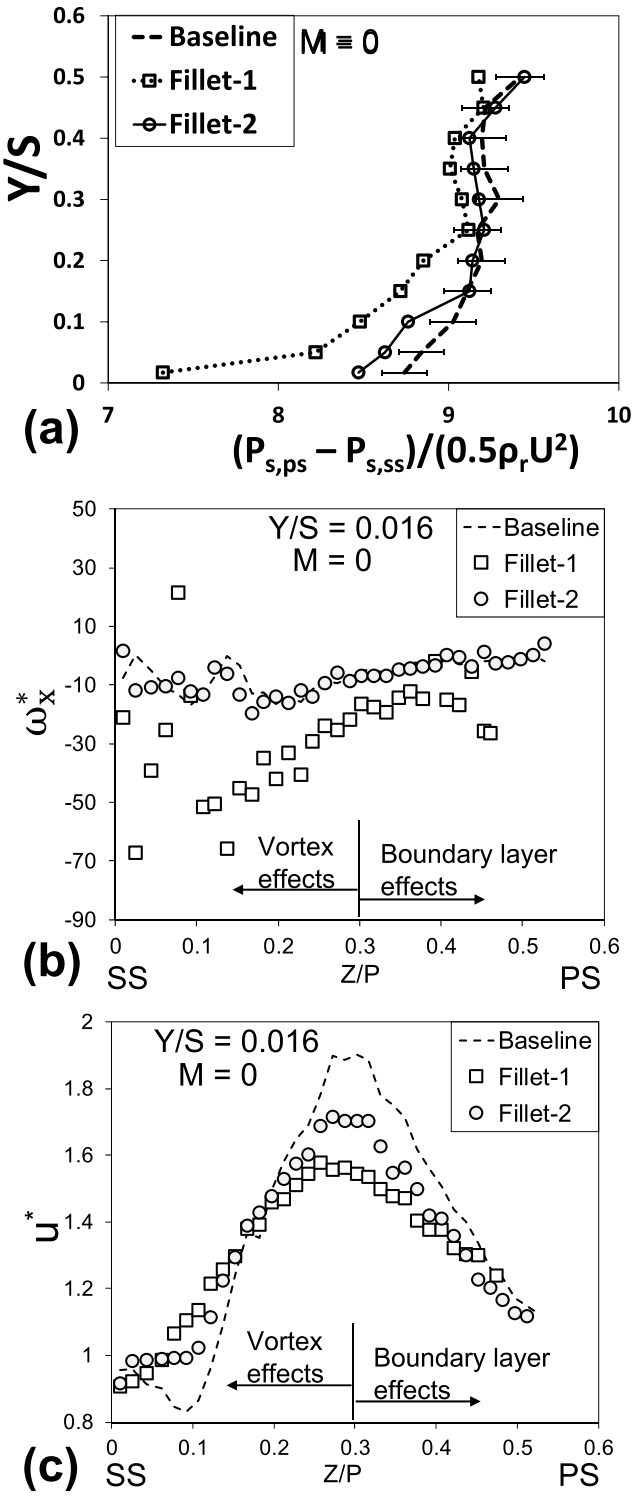


**Figure 12.** Flow data in plane at $X_G/C_{ax} = 0.58$ with and without fillet for $M = 0.0$: (a) pressure difference, $(P_{s,ps} - P_{s,ss})/(0.5\rho_r U^2)$ vs. Y/S, (b) normalized vorticity, $\omega_x^*$ vs. Z/P at Y/S = 0.016, and (c) normalized velocity, u* vs. Z/P at Y/S = 0.016. Error bars are shown on the baseline data in Figure . 9(a).

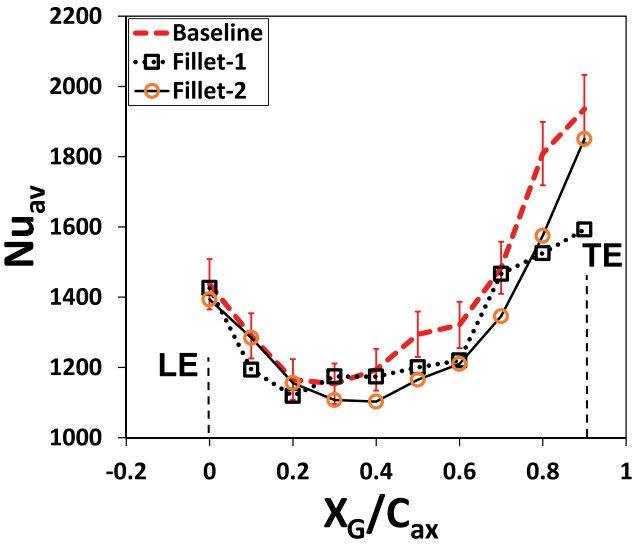


**Figure 13.** Pitch-averaged nusselt number, $Nu_{av}$ distributions along axial $X_G/C_{ax}$ for baseline, fillet-1, and fillet-2 with $M = 0.0$. Error bars are shown on the baseline data.

passage vortex, in the absence of film-cooling flow ($M = 0.0$). The static pressures, $P_{s,ps}$ and $P_{s,ss}$, used to calculate $(P_{s,ps} - P_{s,ss})/(0.5\rho_r U^2)$ in Figure 12(a), are measured in the pitchwise plane at the axial location $X_G/C_{ax} = 0.58$. Error bars are displayed solely on the Baseline data in Figure 12(a) to ensure the clarity of data distribution across all cases. Lower pressure difference values, $(P_{s,ps} - P_{s,ss})$, near the endwall diminish the flow's turn toward the suction side, attenuate the passage vortex, and potentially enhance film-cooling flow distribution as suggested by Li *et al* [40]. The magnitude of $(P_{s,ps} - P_{s,ss})/(0.5\rho_r U^2)$ generally escalates further from the endwall where $Y/S > 0.25$. Elevated pressure differences further from the endwall counterbalance the centrifugal forces acting on the fluid particles, aligning the streamlines with the passage [7], [37]. The normalized pressure differences, $(P_{s,ps} - P_{s,ss})/(0.5\rho_r U^2)$, are consistent at $Y/S > 0.25$ across all cases, but are reduced for the fillets compared to the baseline at $Y/S < 0.25$. The constriction of the flow area on the endwall due to Fillet-1 leads to a decrease in the local static pressure, $P_{s,ps}$, resulting in the smallest values of $(P_{s,ps} - P_{s,ss})/(0.5\rho_r U^2)$ at $Y/S < 0.25$ in Figure 12(a). The area impacted by Fillet-2 in the pressure-side corner at $X_G/C_{ax} = 0.58$ is considerably less extensive than that of Fillet-1. Therefore, the local static pressure, $P_{s,ss}$ , and the values of $(P_{s,ps} - P_{s,ss})/(0.5\rho_r U^2)$ at $Y/S < 0.25$ for Fillet-2 are not as markedly reduced as those for Fillet-1.

Figure 12(b, c) showcase a comparative analysis of the axial vorticity and axial velocity intensities along the endwall for baseline and filleted configurations, excluding film-cooling effects. The data, normalized and plotted along the pitch-line at $Y/S = 0.016$ and axial location $X_G/C_{ax} = 0.58$, utilize Eq. (7) to calculate the normalized axial vorticity, $\omega_x^*$.

$$\omega_x^* = \left(\frac{\partial w}{\partial y} - \frac{\partial v}{\partial z}\right) \cdot \frac{C}{U} \tag{7}$$

The derivatives required for Eq. (7) are numerically derived from the velocity components (v, w) measured in the pitchwise plane. The data are categorized into two zones: (i) the zone at $Z/P < .3$, dominated by the passage-vortex legs, and (ii) the zone at $Z/P > .3$, where boundary layer flow accelerations are more pronounced. According to Figure 12(b), the local $\omega_x^*$ values are notably higher for the Fillet-1 scenario. It's important to note that the total pressure loss distributions, discussed in Section 3.3, more accurately reflect the strength of the three-dimensional passage vortex. In Figure 12(c), the normalized axial velocity, $u^*$ generally exceeds 1.0 away from the suction side (SS), indicating an acceleration of the passage flow relative to the upstream reference velocity, U. The $u^*$

**Table 4.** Comparisons of heat transfer coefficients between present and reference cascades.

| | | 0.0 | 0.3 | 0.6 | 0.0 | 0.3 | 0.6 |
|---|---|---|---|---|---|---|---|
| Un-filleted cascade cases | $X_G/C_{ax}$ = | | *$St_{av}$x$10^3$ | | | *$h_{av}$ (W/$m^2$.K) | |
| Present, $M = 0$, Tu = 3% | | 10 | 8 | 9 | 105 | 86 | 98 |
| Thole et al. [32], Tu = 0.6% | | 5.5 | 6.2 | 7.2 | | | |
| Thole et al. [32], Tu = 19.5% | | 6.7 | 7.3 | 9 | | | |
| Werschnik et al. [33], $M = 0$ | | | | | 140 | 100 | 110 |

*$St_{av}$ = average Stanton number, $h_{av}$ = average convection heat transfer coefficient.

values diminish toward the SS and pressure side (PS) due to the influence of the passage-vortex legs and the boundary layer's presence. The baseline reduction in u* at $Z/P < .15$ is attributed to a more potent passage vortex, while the peak u at $Z/P = .3$ results from increased boundary layer accelerations. This heightened velocity within the boundary layer contributes to an increase in endwall heat transfer. The combined influences of the secondary vortex, $\omega_x^*$ and flow speed, $u^*$ are relatively weaker on the heat transfer for the Fillet-2 in Figure 11(e).

Figure 13 compares the pitchwise-averaged Nusselt number distributions along the passage between the baseline and fillet cases. The average $Nu_{av}$ at a given $X_G/C_{ax}$ location in the figure is determined from the average of local Nusselt numbers along the pitch-line locations, $Z_G/P$ at that particular $X_G/C_{ax}$. The $Nu_{av}$ values are high for all the cases near the LE region of $X_G/C_{ax} = 0$ where the dominating effects of the LE horseshoe vortex and passage-vortex legs increase the local heat transfer on endwall significantly. Downstream of the leading-edge region within $0.0 < X_G/C_{ax} < 0.3$, $Nu_{av}$ values taper off as the influence of endwall secondary flows wanes and the boundary layer's influence grows. Further downstream, the acceleration within the boundary layer begins to affect the $Nu_{av}$.

The rise in the $Nu_{av}$ beyond the axial position $X_G/C_{ax} > 0.3$ along the endwall is primarily due to the pronounced acceleration of the flow within the passage. This pattern of heat transfer distribution, averaged along the pitch-line, aligns with findings from previous studies [32, 38]. Figure 13 reveals that $Nu_{av}$ values are notably lower for Fillet-2 between $0.2 < X_G/C_{ax} < 0.8$, largely because of the reduced intensity of the axial vorticity, $\omega_x^*$, within the boundary layer. Compared to the baseline, $Nu_{av}$ values for Fillet-1 are also reduced as shown in Figure 13. Table 4 juxtaposes the current baseline results without fillets against those from references [32, 38] at equivalent axial positions. For ease of comparison, the baseline $Nu_{av}$ is translated into average Stanton number ($St_{av}$) and heat transfer coefficient ($h_{av}$) in Table 4. Variations in the passage geometry and vane profiles account for the discrepancies observed in the table.

## *Adiabatic effectiveness of film-cooling*

Figures 14 to 18 showcase the adiabatic film-cooling effectiveness, denoted as $\eta$ along the endwall for various film-cooling configurations. The effectiveness $\eta$ is calculated from the measured wall temperatures using Eq. (4), where lower wall temperatures, $T_w$ correspond to higher $\eta$ values. Thus, regions with elevated $\eta$ values indicate more effective coverage and protection of the endwall by the film-cooling flow.

In Figure 14, the distribution of $\eta$ is depicted for the baseline case, which includes all film-cooling holes without any fillets, at blowing ratios $M$ of 1.4 and 2.2. The color legends for the $\eta$ contours are consistent for both blowing ratios, and no color contours are present at the film-cooling slot locations. The contours with $\eta \geq 0.4$ downstream the slots, trace the core regions of the film cooling streams. The effectiveness of the coolant flow from the leading-edge (LE) discrete holes at $M = 1.4$ is also evident in Figure 14. According to Huyssen et al. [34], the $\eta$ distribution with values of 0.4 or higher in the core region of the coolant flow extends downstream beyond the boundary layer separation zone, with the approximate separation lines drawn based on [25].

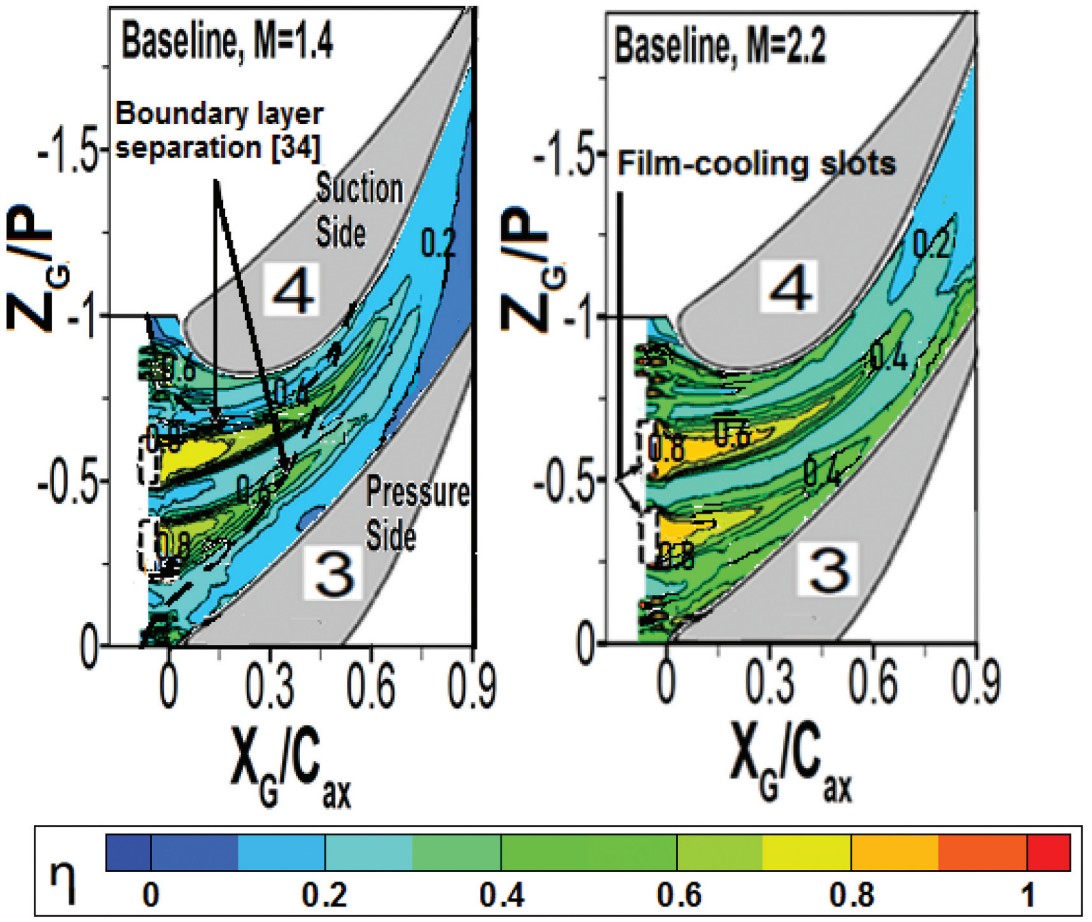


**Figure 14.** Adiabatic film-cooling adiabatic effectiveness, η along endwall for the baseline: $M = 1.4$ and $M = 2.2$.

As the blowing ratio $M$ increases from 1.4 to 2.2, the range of $0.2 \leq \eta \leq 0.4$ extend along the endwall, reflecting the enhanced mass and momentum of the coolant flow at $M = 2.2$.

At $M = 1.4$ the suction-side leg and pressure-side leg vortices capture and overpower the coolant flow from the LE discrete holes. The strong pressure gradient ($P_{s,ps} - P_{s,ss}$) between the PS and SS, as shown in Figure 12(a), along with the elevation of coolant flow by the passage-vortex regions in Figure 8, prevent the uniform distribution of high $\eta$ values for the Baseline case.

Referring to the Nusselt number ($Nu$) distributions in Figure 11(a) for the Baseline, the coolant flows in Figure 14 for both $M = 1.4$ and $M = 2.2$ appear to envelop the high $Nu$ regions with $\eta$ values of 0.2 or greater, located upstream of the passage throat. These high $Nu$ regions correspond to the hotter areas on the endwall. The $\eta$ distributions in Figure 14, which lack fillets, seem to outperform the slot flow cases in Reference [13], particularly along the pressure side. In [13], a substantial portion of the endwall near the entire pressure side of the vane passage exhibits $\eta$ values of 0.2 or lower at low blowing ratios. In contrast, the effectiveness distributions in the same pressure-side endwall region of [13] diminish to nearly zero at higher blowing ratios, unlike the current study where $\eta$ values of 0.2 or greater near the pressure side increase with the blowing ratio. The coolant flow from the 45° slot in [13] draws hot mainstream gases toward the endwall region at higher blowing ratios, thereby reducing the $\eta$ distributions.

Figure 15 presents a comparison of the adiabatic film-cooling effectiveness $\eta$ for Baseline-1, Baseline-2, Fillet-1, and Fillet-2 configurations at a blowing ratio $M = 1.4$. The color legends for the

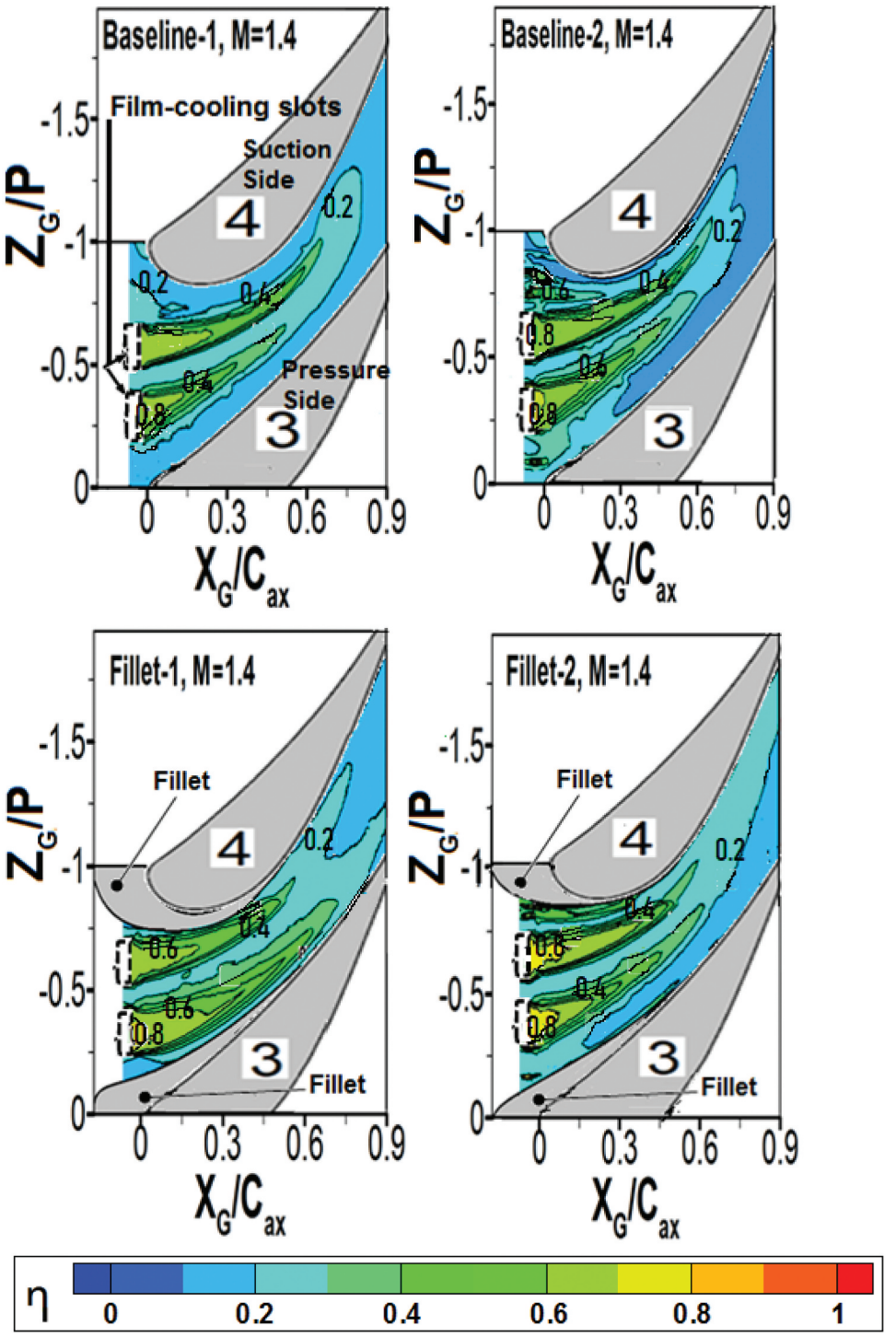


**Figure 15.** Adiabatic film-cooling effectiveness, η at $M = 1.4$ for configurations of: baseline-1, baseline-2, fillet-1, and fillet-2. Fillet and film-cooling slot positions are marked.

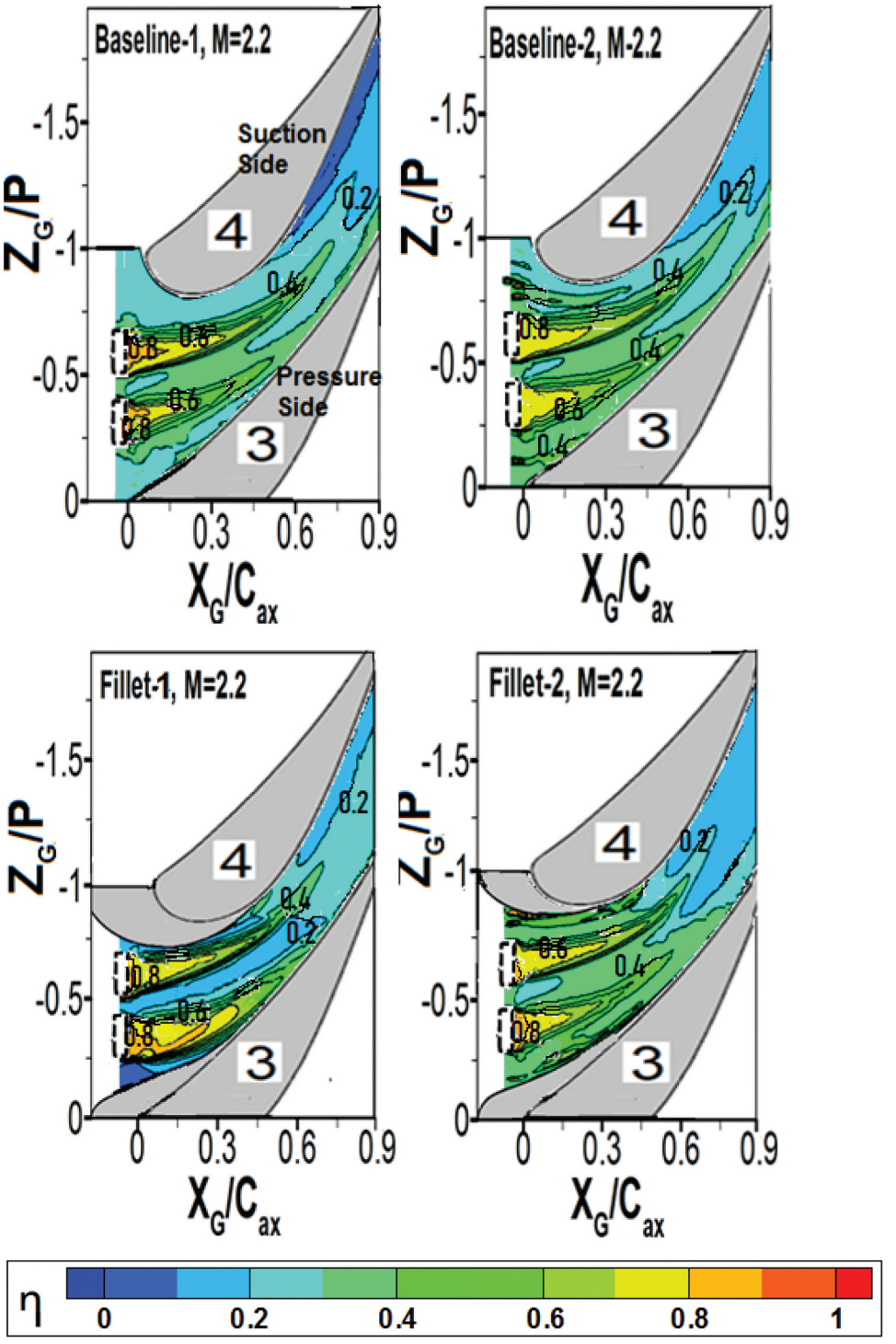


**Figure 16.** Adiabatic film-cooling effectiveness, η along endwall at $M = 2.2$ for configurations of: baseline-1, baseline-2, fillet-1, and fillet-2.

$\eta$ contours are provided at the bottom of the figure, and the fillet regions are marked by a uniform gray area where no data is displayed. The figure reveals that the area with $\eta \geq 0.2$ is more extensive along the endwall for Baseline-2 compared to Baseline-1, largely due to the coolant emerging from the open film-cooling holes near the leading edge (LE). The baseline scenario in Figure 14 (at $M = 1.4$) exhibits marginally greater $\eta$ values than those seen in Baseline-1 and Baseline – 2 in Figure 15, which is attributed to the coolant discharged from all LE discrete holes and a less intense passage vortex core.

In terms of the filleted configurations in Figure 15, the $\eta \geq 0.4$ downstream of the slots are more widely distributed in the pitchwise direction for Fillet-1. The variance in $\eta$ values between the two filleted cases can be explained by (i) the reduced pitchwise pressure differential ($P_{s,ps}$- $P_{s,ss}$) near the endwall for Fillet-1 compared to Fillet-2, as shown in Figure 12(a), which directs more coolant flow along the pressure side of Fillet-1, and (ii) the elevated position of the passage vortex in the Fillet-2 case (as depicted in Figure 9(d)) which diverts some of the coolant flow away from the endwall. Consequently, due to the aforementioned reason (i), Fillet-1 also achieves higher $\eta$ values along the endwall relative to Baseline-1 and Baseline-2.

When the blowing ratio $M$ is raised to 2.2 in Figure 16 for Baseline-1, Baseline-2, and Fillet-1, Fillet-2, there is an observed increase in the spread of $\eta \geq 0.2$ along the endwall, particularly downstream of the cooling slots, across all configurations. However, in the case of Fillet-1, the $\eta$ values near the pressure side and the central pitchwise positions are reduced in Figure 16 compared to Figure 15, which is attributed to a greater volume of coolant being lifted off the endwall, as demonstrated in Figure 10. Out of all scenarios presented in Figure 16, Fillet-2 exhibits the highest $\eta$ values. The

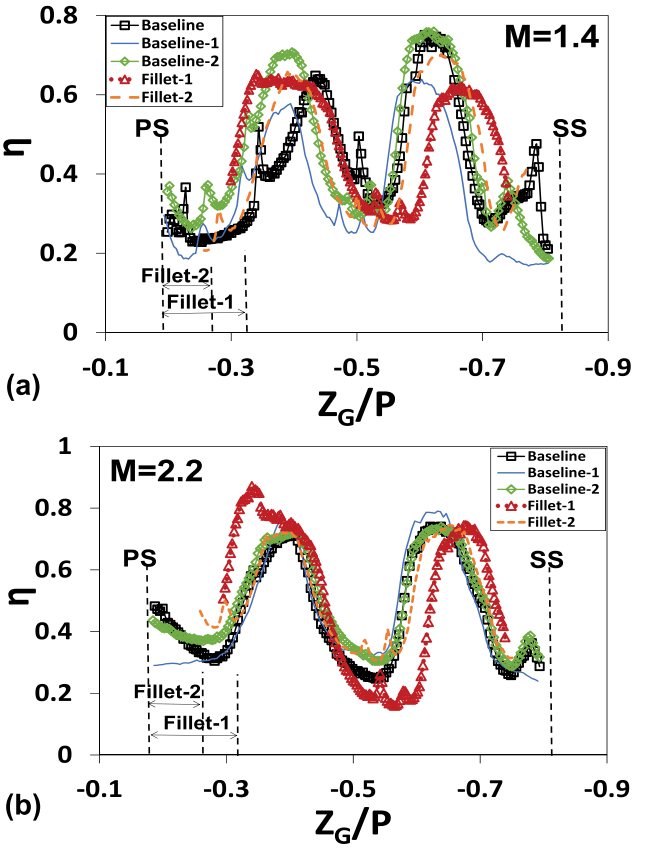


**Figure 17.** Local adiabatic effectiveness, η vs. pitchwise $Z_G/P$ at $X_G/C_{ax} = 0.15$ for baseline, baseline-1, baseline-2, fillet-1, and fillet-2: (a) $M = 1.4$ and (b) $M = 2.2$.

baseline scenario in Figure 14 (at $M = 2.2$) shows greater $\eta$ values than those in Figure 16, thanks to the coolant emerging from the leading-edge (LE) discrete holes. The $\eta$ values at $M = 2.2$ are significantly influenced by the elevation of the coolant flow in all cases. Consequently, Fillet-1 achieves the most favorable $\eta$ distributions at $M = 1.4$ as seen in Figure 15, while Fillet-2 attains the best $\eta$ distributions at $M = 1.2$ in Figure 16.

The local pitchwise $\eta$ distributions along $Z_G/P$ in Figures 17 and 18 are derived from the data in Figures 10 and 14. 14 to 15 at two axial locations $X_G/C_{ax} = 0.15$ and 0.58. The data in Figures 17 and 18 assess the pitchwise uniformity of $\eta$ distributions for all film-cooling scenarios at blowing ratios $M = 1.4$ and 2.2. For the filleted configurations, no data is presented at the locations marked for Fillet-1 and Fillet-2. At $X_G/C_{ax} = 0.15$ in Figure 17, the $\eta$ distributions exhibit noticeable variations and non-uniformity, as indicated by peaks and troughs between the pressure side (PS) and suction side (SS) for all configurations. The disparity in $\eta$ values between these peaks and troughs is substantial, owing to the boundary layer separation areas and the limited coolant flow, which hinders adequate coolant from reaching the vicinity of the PS and SS. Additionally, the coolant flow is diminished downstream of the gaps between the slots. The minor peaks in $\eta$ values near the SS in Figure 17 result from the coolant discharged from the LE discrete holes in the Baseline, Baseline-2, and Fillet-2 cases. At $X_G/C_{ax} = 0.58$ in Figure 18, the variations in $\eta$ values between the peaks and troughs are considerably less pronounced than those in Figure 17. The troughs in $\eta$ values in Figure 18 primarily stem from the reduced coolant flow downstream of the slot gaps. The variation in $\eta$ values lessens in Figure 18 as the

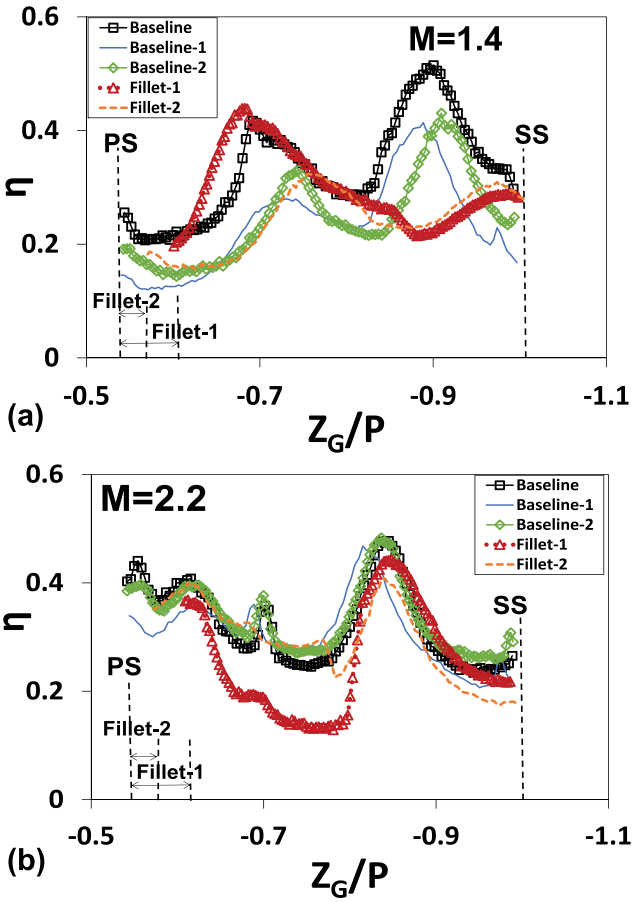


**Figure 18.** Local adiabatic effectiveness, η vs. pitchwise $Z_G/P$ at $X_G/C_{ax} = 0.58$ for baseline, baseline-1, baseline-2, fillet-1, and fillet-2: (a) $M = 1.4$ and (b) $M = 2.2$.

blowing ratio $M$ increases from 1.4 to 2.2. The Fillet-2 configuration provides the most uniform $\eta$ distributions in Figure 18.

The local film-cooling effectiveness $\eta$, is averaged across the pitch at fixed axial positions, denoted as $X_G/C_{ax}$. These pitchwise-averaged values, $\eta_{pitch\text{-}av}$, are then graphed against the axial locations in Figure 19 for blowing ratios $M = 1.4$ and 2.2, allowing for a comparison across all film- cooling configurations. The trend depicted shows a decline in $\eta_{pitch\text{-}av}$ as the axial distance increases, reflecting the downstream reduction in coolant distribution. The baseline configuration exhibits the highest $\eta_{pitch\text{-}av}$, with Fillet-1 at $M = 1.4$ closely aligning with these values. Baseline-1 at $M = 1.4$ has the lowest $\eta_{pitch\text{-}av}$ since it only receives coolant from two slots. At a higher blowing ratio of $M = 2.2$, Fillet-2 achieves the highest $\eta_{pitch\text{-}av}$ values in regions where $X_G/C_{ax}$ <0.5. Beyond $X_G/C_{ax} = 0.5$, the differences in $\eta_{pitch\text{-}av}$ among the configurations are minimal.

Figure 20(a) presents the arithmetic mean of all local $\eta$ values from $X_G/C_{ax} = 0.5$ to 0.9. These averages, $\eta_{av}$ , are compared as the blowing ratio $M$ varies from 1.0 to 2.8 among the different film-cooling configurations. Higher local effectiveness is observed at $X_G/C_{ax}$ <0.5 for all cases. Thus, the data in Figure 20 offer a more comprehensive comparison, highlighting where the influence of passage vortex structures on endwall heat transfer is most and least pronounced. Significant coolant liftoff is noted at $X_G/C_{ax} = 0.58$ in Figures 8 and 10, suggesting that the coolant remains attached to the endwall below $X_G/C_{ax} = 0.58$. As expected, $\eta_{av}$ rises with increasing $M$ for all configurations, with the baseline showing the highest $\eta_{av}$ in both Figure 20(a,b), followed by Baseline-2. However, the increase in $\eta_{av}$ is

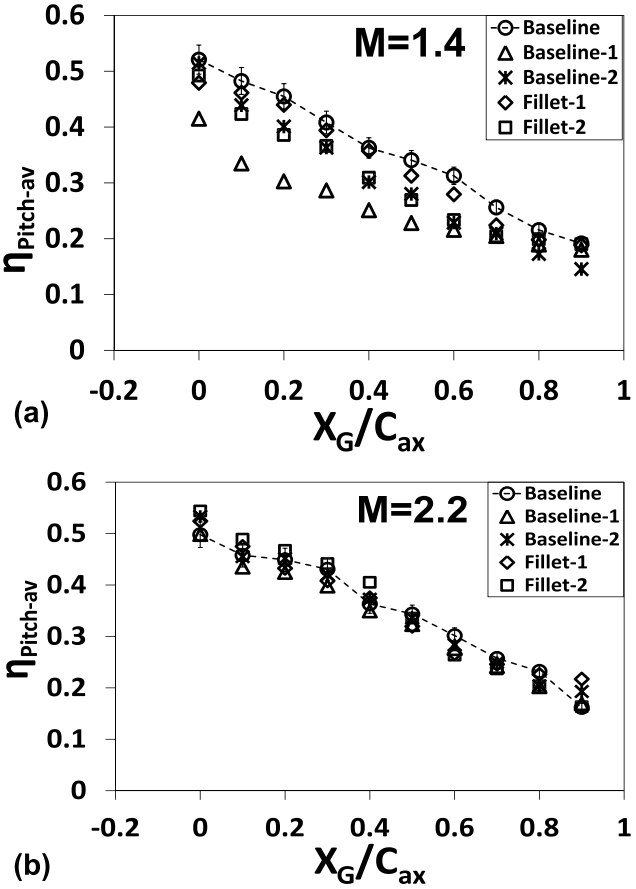


**Figure 19.** Pitchwise-averaged adiabatic effectiveness, $\eta_{av}$ vs. axial $X_G/C_{ax}$ for five film-cooling cases: (a) $M = 1.4$ and (b) $M = 2.2$. Error bars are shown on the baseline data.

marginal when $M > 1.8$, mainly due to the reduced penetration of coolant into the boundary layer. The lowest $\eta_{av}$ distributions are for Baseline-1 in Figure 20(a) and for Fillet-2 in Figure 20(b), underscoring the discernible impact of the fillet and LE film-cooling holes.

The study does not explore the effects of freestream turbulence exceeding 3% on current film-cooling effectiveness. However, based on positive outcomes from high freestream turbulence in Refs [10, 36], it's anticipated that the lateral adiabatic effectiveness distributions in the vane cascade would also improve with increased upstream turbulence. This enhancement could occur as the elevated turbulent kinetic energy imparts additional momentum to the film-cooling flow, helping it counteract the pitchwise pressure gradient and passage vortex to some degree. Near and downstream of the throat, where freestream turbulence significantly drops due to acceleration of the flow, the beneficial impact of high turbulence on effectiveness is expected to diminish. Yet, if high turbulence levels are induced through vortex or swirl motions in the freestream, the local effectiveness distributions might substantially decrease in the pitchwise center of the cascade, similar to findings in [38, 41]. The mass flux and momentum of the film-cooling flow at a given blowing ratio rise with the density ratio. Changes in the density ratio do not affect the jet velocity in the film-cooling holes and slots. Therefore, the pitchwise effectiveness distributions for the current film-cooling scenarios are projected to increase with the density ratio, as reported in Refs [40, 42, 43].

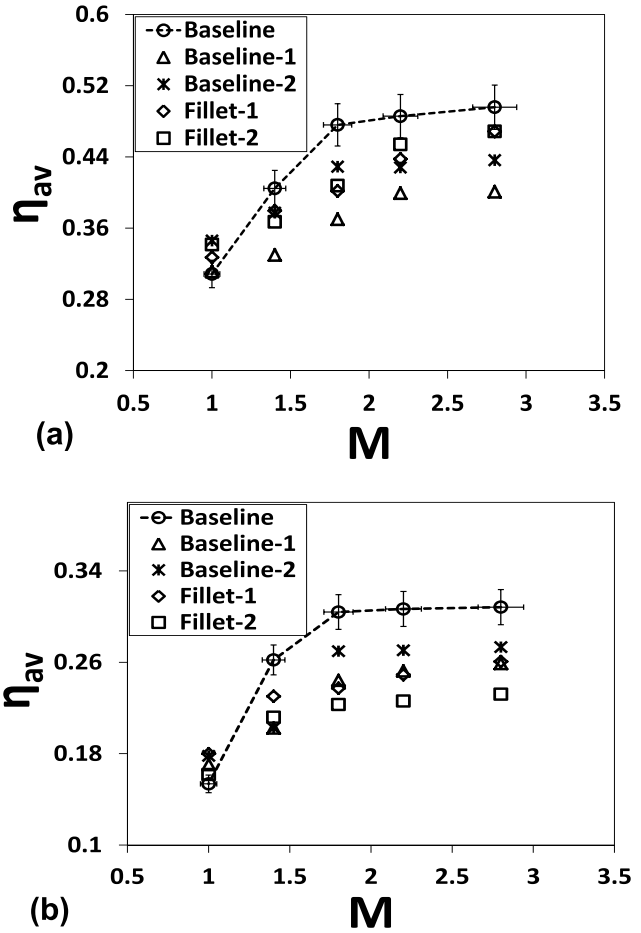


**Figure 20.** Globally-averaged adiabatic effectiveness, $\eta_{av}$ vs. M for five film-cooling cases: (a) averaged in $0.0 \le X_G \le 0.50$ and (b) averaged in $0.5 \le X_G \le 0.90$. Error bars are shown on the baseline data.

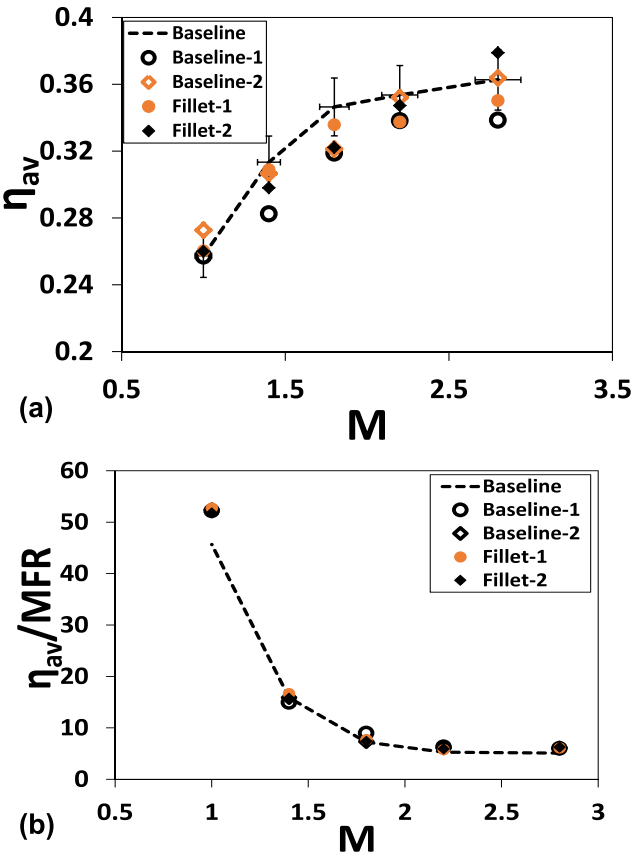


**Figure 21.** (a) Globally averaged $\eta_{av}$ vs. M for five film-cooling cases in region of $0.0 \le X_G \le 0.90$, and (b) globally averaged ($\eta_{av}$/MFR) vs. M. Error bars are shown on the baseline data in (a).

The average film-cooling effectiveness, $\eta_{av}$ shown in Figure 21 is derived from the arithmetic mean of all local $\eta$ values within the range of $0.0 \le X_G/C_{ax} \le 0.9$. As depicted in Figure 21(a), the variation in $\eta_{av}$ with increasing blowing ratio $M$ is minimal across the film-cooling configurations of Baseline, Baseline-2, and Fillet-1. These $\eta_{av}$ values are normalized by the coolant mass fraction ratios ($MFR$) from Table 3 and plotted in Figure 21(b) against the blowing ratios $M$. The baseline configuration has the highest $MFR$ values for all blowing ratios according to Table 3.

In practical gas turbine applications, a lower $MFR$ is preferred for a given $M$ to reduce the compressor load needed for coolant delivery. Therefore, higher ratios of $\eta_{av}$ to $MFR$ indicate better adiabatic film-cooling effectiveness. The ratio of adiabatic film cooling effectiveness to mass flow rate depicts the efficiency of the cooling system in relation to the quantum of coolant being supplied. This ensures that turbine components are sufficiently cooled while minimizing the energy consumption associated with coolant delivery. The ratios of $\eta_{av}$ to $MFR$ in Figure 21(b) are similar for all film- cooling configurations but show a marked decrease from $M = 1.0$ to $M = 1.8$. This decline is due to the significant increase in MFR with the blowing ratio, leading to a steep drop in $\eta_{av}$ to $MFR$ ratios. Consequently, the baseline configuration, as illustrated in Figures 20 and 21, achieves higher $\eta_{av}$ values but at the cost of increased film-cooling flow rates. Conversely, the Fillet-1 and Fillet-2 configurations attain comparable $\eta_{av}$ to $MFR$ values at the baseline but with lower film- cooling flow rates. Overall,

the best injection condition is Fillet-2 with a better uniform pitchwise-distributions of the film-cooling effectiveness

## Conclusions

The experimental distributions of pressure loss, endwall heat transfer, and endwall adiabatic effectiveness of film-cooling are presented in a linear cascade employing filleted vanes and discrete slots and holes of film-cooling. Two fillet profiles (Fillet-1 and Fillet-2) are tested. The discrete slots and discrete cylindrical holes are employed just upstream of the cascade inlet. The blowing ratio of film-cooling flow varies between 1.0 and 2.8. The measurements are also presented without the fillets when the film-cooling configurations are open fully (Baseline case) as well as open partially (Baseline-1 and Baseline-2 cases). The primary objectives of the investigation are to illustrate the effects of filleted vanes on the endwall heat transfer and film-cooling effectiveness.

The pressure distributions show the filleted cases reduce the pressure differences between the pressure side and suction side of the passage near the endwall. As a consequence, the total pressure loss coefficients and size of the passage vortex core are smaller for the filleted cases than for the baseline case (no fillet) without the film-cooling. The local Nusselt number distributions are also smaller for the filleted passage than for the no-fillet baseline passage. When the results are compared between the two fillet profiles, the total pressure loss coefficients in the passage vortex and Nusselt numbers are slightly smaller for the Fillet-2 than for the Fillet-1. The coolant flow lifts off the endwall and mixes with endwall region flow when the blowing ratio of film-cooling flow is high. The passage vortex region and total pressure loss coefficients of the passage vortex decrease with the film-cooling flow for the baseline cases (Baseline, Baseline-1, Baseline-2) and Fillet-1. For the Fillet-2, both the passage vortex and total pressure losses of passage vortex increase with the film-cooling.

The endwall adiabatic effectiveness of film-cooling show that all of the five film-cooling configurations provide cooling of the high Nusselt number regions on endwall. The film-cooling effectiveness goes past the boundary layer separation regions for all the blowing ratios of film- cooling. The effectiveness values are the highest for the baseline case employing all slots and holes of film-cooling. With the film-cooling holes blocked, the effectiveness distributions are higher for the Fillet-1 at low blowing ratios and higher for the Fillet-2 at higher blowing ratios. Fillet-2 also provides better uniform pitchwise-distributions of the film-cooling effectiveness. The ratio of overall-average effectiveness to coolant mass-fraction-ratio for all the five-cases are about the same for all the blowing ratios. The filleted vanes thus provide the ratios of film-cooling effectiveness to mass-fraction comparable to the baseline cases and use lower film-cooling flow rates.

## Nomenclature

| | |
|---|---|
| $A_{heater}$ | Wall-heater area |
| C, $C_{ax}$ | Vane profile actual and axial chord |
| $C_{p,b}$, $C_{Pt,loss}$ | Pressure coefficient: vane-wall and total-loss |
| L, W | Film-cooling slot length and width |
| LE, TE | Leading edge and trailing edge of vane |
| M, (MFR) | Inlet blowing ratio (BR) and mass fraction ratio of coolant |
| $M_a$, $M_c$ | Mass flow rate in single passage: main flow and coolant flow |
| Nu | Endwall Nusselt number |
| P, S | 2-dimensional vane pitch and span |
| PS, SS | Passage pressure side and suction side |
| $P_b$ | Local pressure on vane profile |
| $P_{s,ps}$, $P_{s,ss}$ | Static pressure near pressure and suction side |
| $P_{s,r}$, $P_{t,r}$ | Reference pressure: static and total |
| $P_{t,b}$ | Total pressure inside plenum box |

| | |
|---|---|
| $P_{heater}$ | Electric power into wall heater, (voltage*current) |
| $Q_{conv}$, $Q_{cond}$ | Convection power and conduction-loss power |
| Re | Inlet Reynolds number to cascade, ($\rho_r UC/\mu$) |
| $T_{c,b}$, $\rho_{c,b}$ | Air temperature and density in coolant plenum |
| $T_r$, $T_a$ | Air temperature: freestream and local |
| $T_w$ | Local endwall temperature |
| U | Reference freestream velocity along $X_G$ |
| (X, Y, Z) | Local Cartesian coordinates |
| ($X_G$, $Y_G$, $Z_G$) | Global coordinates |
| d | Rod diameter of turbulence grid |
| b | Streamline distance between two rows of holes |
| $k_{air}$ | Thermal conductivity of air |
| s | Distance along vane profile from leading-edge |
| (u, v, w) | Local velocity components along (X, Y, Z) |
| u* | Normalized axial velocity, (u/U) |
| *Greeks* | |
| $\delta$, $\delta_T$ | Boundary layer thickness: velocity and temperature |
| $\eta$ | Local adiabatic local film-cooling effectiveness |
| $\eta_{pitch\text{-}av}$, $\eta_{av}$ | Average adiabatic film-cooling effectiveness: pitchwise and global |
| $\mu$, $\rho_r$ | Air density and viscosity in reference plane |
| $\omega_x^*$ | Normalized axial vorticity |

## Acknowledgments

The authors are grateful for the financial contributions of the National Research Foundation (NRF) of South Africa (NRF Grant No: 91013 and 95777).

## Disclosure statement

No potential conflict of interest was reported by the author(s).

## References

[1] Ö. H. Turgut and C. Camci, "A simultaneous use of a leading-edge fillet and a non-axisymmetrically contoured endwall in a turbine stage," *Aerosp. Sc. Technol*, vol. 118, no. 106985, pp. 106985, 2021. DOI: 10.1016/j.ast.2021.106985.

[2] K. Du, X. Pei, X. Shan, Z. Zhao, and C. Liu, "Influence of the slot fillet and vane root fillet on the turbine vane endwall cooling performance," *Machine*, vol. 11, no. 7, pp. 729, 2023. DOI: 10.3390/machines11070729.

[3] Y. Zhang, X. Yuan, and P. Ligrani, "Film cooling effectiveness distribution on first-stage vane endwall with and without leading-edge fillets," *Int. J. Heat Mass Tran.*, vol. 66, pp. 642–654, 2013. DOI: 10.1016/j.ijheatmasstransfer.2013.06.065.

[4] G. I. Mahmood and K. Arnachellan, "Effects of upstream endwall film-cooling on a vane cascade flow-field," *J. Propul. Power*, vol. 34, no. 2, pp. 460–468, 2018. DOI: 10.2514/1.B36640.

[5] G. I. Mahmood and K. Arnachellan, "Flow-field in a linear vane cascade with endwall fillet and film-cooling, published by ASME," Proc. ASME 2018 5th Joint US-European Fluids Engr Summer Conf. ASME Paper No. FEDSM2018-83140, July 15–20, 2018, Montreal, Quebec, Canada., 2018, pp. V002T11A004. https://doi.org/10.1115/FEDSM2018-83140.

[6] A. S. Shote, G. I. Mahmood, and J. P. Meyer, "Influences of large fillets on endwall flows in a vane cascade with upstream slot film-cooling," *Exp. Therm. Fluid Sci.*, vol. 112, pp. 109951, 2020. DOI: 10.1016/j.expthermflusci.2019.109951.

[7] M. Thomas and T. Povey, "Improving turbine endwall cooling uniformity by controlling near-wall secondary flows," Proceedings of the Institution of Mechanical Engineers, Part G: Journal of Aerospace Engineering., vol. 231, pp. 2689–2705, 2017. DOI: 10.1177/0954410016673092.

[8] F. Ornano and T. Povey, "Experimental and computational study of the effect of momentum-flux ratio on high-pressure nozzle guide vane endwall cooling system," *J. Turbomach.*, vol. 139, no. 12, pp. 1210021–12100214, 2017. DOI: 10.1115/1.4037756.

[9] W. Colban and K. A. Thole, "Influence of hole shape on the performance of a turbine vane endwall film-cooling scheme," *Int. J. Heat Fluid Flow*, vol. 28, no. 3, pp. 341–356, 2007. DOI: 10.1016/j.ijheatfluidflow.2006.05.002.

[10] W. Colban, K. A. Thole, and M. Haendler, "A comparison of cylindrical and fan-shaped film-cooling holes on a vane endwall at low and high freestream turbulence levels." *J. Turbomach.*, vol. 130, no. 3, pp. 031007–031009, 2008. DOI: 10.1115/1.2720493.
[11] G. Barigozzi, G. Franchini, and A. Perdichizzi, "End-wall film cooling through fan-shaped holes with different area ratios," *J.Turbomachinery*, vol. 129, no. 2, pp. 212–220, 2007. DOI: 10.1115/1.2464140.
[12] N. Wang, C.-C. Shiau, J.-C. Han, H. Xu, and M. Fox, "Turbine vane endwall film cooling from mid-chord or downstream rows and upstream coolant injection," *Int. J. Heat Mass Tran.*, vol. 133, pp. 247–255, 2019. DOI: 10.1016/j.ijheatmasstransfer.2018.12.079.
[13] K. A. Thole and D. G. Knost, "Heat transfer and film-cooling for the endwall of a first stage turbine vane," *Int. J. Heat Mass Tran.*, vol. 48, no. 25–26, pp. 5255–5269, 2005. DOI: 10.1016/j.ijheatmasstransfer.2005.07.036.
[14] S. Hada and K. A. Thole, "Computational study of a midpassage gap and upstream slot on vane endwall film-cooling." *J. Turbomach.*, vol. 133, no. 1, pp. 011024–011029, 2011. DOI: 10.1115/1.4001135.
[15] K. Du and J. Li, "Numerical study on the effects of slot injection configuration and endwall alignment mode on the film cooling performance of vane endwall," *Int. J. Heat Mass Tran.*, vol. 98, pp. 768–777, 2016. DOI: 10.1016/j.ijheatmasstransfer.2016.02.014.
[16] G. Barigozzi, H. Abdeh, A. Perdichizzi, M. Henze, and J. Krueckels, "Aerothermal performance of a nozzle vane cascade with a generic nonuniform inlet flow condition—part II: influence of purge and film cooling injection," *J. Turbomach.*, vol. 139, no. 10, pp. 1010041–1010049, 2017. DOI: 10.1115/1.4036437.
[17] Z. Tao, Y. Yao, P. Zhu, L. Song, and J. Li, "Experimental and numerical study on film cooling effectiveness of an annular cascade endwall with different slot configuration," *Int. J. Therm. Sci.*, vol. 158, pp. 106517, 2020. DOI: 10.1016/j.ijthermalsci.2020.106517.
[18] N. Sundaram and K. A. Thole, "Film-cooling flowfields with trenched holes on an endwall." *J.Turbomachinery*, vol. 131, no. 4, pp. 1–10, 2009. DOI: 10.1115/1.3068316.
[19] H. Gao, X. Li, and J. Ren, "Effect of leakage flow on the endwall cooling performance in high subsonic turbine cascade," *Int. J. Therm. Sci.*, vol. 170, pp. 107140, 2021. DOI: 10.1016/j.ijthermalsci.2021.107140.
[20] A. A. Thrift, K. A. Thole, and S. Hada, "Effects of orientation and position of the combustor-turbine interface on the cooling of a vane endwall." *J.Turbomachinery*, vol. 134, no. 6, pp. 061019–061010, 2012. DOI: 10.1115/1.4004817.
[21] B. Laveau, R. S. Abhari, M. Crawford, and E. Lutum, "High resolution heat transfer measurements on the stator endwall of an axial turbine," *J.Turbomachinery*, vol. 137, no. 4, pp. 041005–041011, 2015. DOI: 10.1115/1.4028431.
[22] M. B. Kang, A. Kohli, and K. A. Thole, "Heat transfer and flowfield measurements in the leading edge region of a stator vane endwall." *J.Turbomachinery*, vol. 121, no. 3, pp. 558–568, 1999. DOI: 10.1115/1.2841351.
[23] L. P. Timko, "Energy efficient engine high pressure turbine component test performance report, contract report NASA CR-168289," Jan 1984.
[24] K. Arnachellan, "Aerodynamic Loss Reduction in a Vane Cascade with Leading-Edge Fillet and Upstream Endwall Film-Cooling." M. Thesis, University of Pretoria, Pretoria, South Africa, 2017.
[25] B. B. Huyssen, A. S. Shote, and G. I. Mahmood, "Upstream endwall film-cooling in a vane cascade with cylindrical shape holes," *J. Thermophys. Heat Transf.*, vol. 37, no. 3, pp. 676–689, 2023. DOI: 10.2514/1.T6607.
[26] A. T. Lethander, K. A. Thole, G. Zess, and J. Wagner, "Vane-endwall junction optimization to reduce turbine vane passage adiabatic wall temperatures," *J. Propul. Power*, vol. 20, no. 6, pp. 1096–1104, 2004. DOI: 10.2514/1.3887.
[27] K. Ananthakrishnan and M. Govardhan, "Influence of fillet shapes on secondary flow field in a transonic axial flow turbine stage," *Aerosp. Sci. Technol*, vol. 82, pp. 425–437, 2018. DOI: 10.1016/j.ast.2018.08.040.
[28] S. R. Sargent, C. R. Hedlund, and P. M. Ligrani, "An infrared thermography imaging system for convective heat transfer measurements in complex flows, Meas," *Meas. Sci. Technol.*, vol. 9, no. 12, pp. 1974–1981, 1998. DOI: 10.1088/0957-0233/9/12/008.
[29] R. J. Moffat, "Describing the uncertainties in experimental result," *Exp. Therm. Fluid Sci.*, vol. 1, no. 1, pp. 3–17, 1988. DOI: 10.1016/0894-1777(88)90043-X.
[30] T. G. Beckwith, R. D. Marangoni, and J. H. Lienhard, *Mechanical Measurements*, 6th ed. New Jersey: Pearson Prentice Hall, 2007, pp. 42–45, 54–59.
[31] P. E. Roach, "The generation of nearly isotropic turbulence by means of grids, heat and fluid flow," *Int. J. Heat Fluid Flow*, vol. 8, no. 2, pp. 82–92, 1987. DOI: 10.1016/0142-727X(87)90001-4.
[32] K. A. Thole, R. W. Radomsky, M. B. Kang, and A. Kohli, "Elevated freestream turbulence effects on heat transfer for a gas turbine vane," *Int. J. Heat Fluid Flow*, vol. 23, no. 2, pp. 137–147, 2002. DOI: 10.1016/S0142-727X(01)00145-X.
[33] H. Werschnik, T. Ostrowski, J. Hilgert, M. Schneider, and H.-P. Schiffer, "Infrared thermography to study endwall cooling and heat transfer in turbine stator vane passages using the auxiliary wall method and comparison to numerical simulations," *Quant. Infrared Thermogr. J.*, vol. 12, no. 2, pp. 219–236, 2015. DOI: 10.1080/17686733.2015.1066135.

[34] S. Han and R. J. Goldstein, "Heat transfer study in a linear turbine cascade using a thermal boundary layer measurement technique," *J. Heat Transf.*, vol. 129, no. 10, pp. 1384–1394, 2007. DOI: 10.1115/1.2754972.
[35] R. W. Radomsky and K. A. Thole, "High free-stream turbulence effects on endwall heat transfer for a gas turbine stator vane," *J.Turbomachinery*, vol. 122, no. 4, pp. 699–708, 2000. DOI: 10.1115/1.1312807.
[36] S.-J. Li, J. Lee, J.-C. Han, L. Zhang, and H.-K. Moon, "Influence of mainstream turbulence on turbine blade platform cooling from simulated swirl purge flow," *Appl. Therm. Eng.*, vol. 101, pp. 678–685, 2016. DOI: 10.1016/j.applthermaleng.2016.01.056.
[37] K. Du, Z. Li, and J. Li, "Effects of the leading edge injection slot on the film cooling and heat transfer performance of the vane endwall," *Int. J. Heat Mass Tran.*, vol. 102, pp. 1308–1320, 2016. DOI: 10.1016/j.ijheatmasstransfer.2016.07.033.
[38] H. Werschnik, H.-P. Schiffer, and C. Steinhausen, "Robustness of a turbine endwall film cooling design to swirling combustor inflow," *J. Propul. Power*, vol. 33, no. 4, pp. 917–926, 2017. DOI: 10.2514/1.B36138.
[39] G. I. Mahmood, R. Gustafson, and S. Acharya, "Experimental investigation of flow structure and nusselt number in a low-speed linear blade passage with and without leading-edge fillets," *J. Heat Transf.*, vol. 127, no. 5, pp. 499–512, 2005. DOI: 10.1115/1.1865218.
[40] X. Li, J. Ren, and H. Jiang, "Film cooling effectiveness distribution of cylindrical hole injections at different locations on a vane endwall," *Int. J. Heat Mass Tran.*, vol. 90, pp. 1–14, 2015. DOI: 10.1016/j.ijheatmasstransfer.2015.06.026.
[41] Z. Gao, D. P. Narzary, S. Mhetras, and J. C. Han, "Upstream vortex effect on turbine platform film cooling with typical purge flow," *J. Thermophys. Heat Tran.*, vol. 26, no. 1, pp. 75–84, 2012. DOI: 10.2514/1.42411.
[42] X. Li, J. Ren, and H. Jiang, "Influence of different film cooling arrangements on endwall cooling," *Int. J. Heat Mass Tran.*, vol. 102, pp. 348–359, 2016. DOI: 10.1016/j.ijheatmasstransfer.2016.06.047.
[43] W. Choi, K. J. Jung, and J. S. Park, "Characteristics of heat transfer on a turbine blade endwall under various inlet flow conditions." *Exp. Heat Transf.*, vol. 34, no. 7, pp. 678–694, 2021. DOI: 10.1080/08916152.2020.1811804.